An *Adnp* frameshift variant disrupts Wnt signalling inducing chromatocytoskeletal defects and autism-related behaviour in male mice

Claudio Peter D'Incal,[a,*] Elisa Cappuyns,[a] Flora Paldi,[b] Mathijs B. van der Lei,[a] Dale John Annear,[a] Clara Milián Alastruey,[c,d] Dimitra Sokolova,[c,d] Ellen Elinck,[a] Kevin De Man,[a] Anthony Konings,[a] Jolien Huyghebaert,[a] Sofie Thys,[e,f] Isabel Pintelon,[e,f] Marlies Verschuuren,[e,f] Elke Calus,[g,h] Debby Van Dam,[g,h] Peter P. De Deyn,[g,h,i,j] Sylvie Nguyen,[k] Binnaz Yalcin,[k,l] Takuro Horii,[m] Izuho Hatada,[m] Ligia Mateiu,[a] Giacomo Cavalli,[b] Emanuela Pasciuto,[c,d] Wim Vanden Berghe,[n] and R. Frank Kooy[a]

[a]Cognitive Genetics (CONGET), Department of Biomedical Sciences, University of Antwerp, Antwerp, Belgium
[b]Institute of Human Genetics, CNRS, University of Montpellier, Montpellier, France
[c]VIB Center for Molecular Neurology, VIB, Antwerp, Belgium
[d]Department of Biomedical Sciences, University of Antwerp, Antwerp, Belgium
[e]Laboratory of Cell Biology and Histology, Department of Veterinary Sciences, University of Antwerp, Antwerp, Belgium
[f]Antwerp Centre for Advanced Microscopy (ACAM), University of Antwerp, Antwerp, Belgium
[g]Laboratory of Neurochemistry and Behavior, Experimental Neurobiology Unit, Department of Biomedical Sciences, University of Antwerp, Antwerp, Belgium
[h]Department of Neurology and Alzheimer Research Center, University of Groningen, and University Medical Centre Groningen (UMCG), Groningen, the Netherlands
[i]Department of Neurology and Memory Clinic, Hospital Network Antwerp (ZNA) Middelheim and HogeBeuken, Antwerp, Belgium
[j]Institute Born-Bunge (IBB) Neurobiobank, University of Antwerp, Antwerp, Belgium
[k]Université Bourgogne Europe, INSERM Research Center U1231, 21070, Dijon, France
[l]Institut NeuroMyoGène, Unité Physiopathologie et Génétique du Neurone et du Muscle, CNRS UMR 5261, Inserm U1315, Université Claude Bernard Lyon 1, 69008, Lyon, France
[m]Laboratory of Genome Science, Biosignal Genome Resource Center, Institute for Molecular and Cellular Regulation, Gunma University, Gunma, Japan
[n]Cell Death Signalling - Epigenetics lab, Department of Biomedical Sciences, University of Antwerp, Antwerp, Belgium

eBioMedicine
2026;128: 106309
Published Online 28 May 2026
https://doi.org/10.1016/j.ebiom.2026.106309

Summary

Background Heterozygous *de novo* variants in the transcription factor *Activity-Dependent Neuroprotective Protein (ADNP)* cause a severe neurodevelopmental disorder, termed Helsmoortel-Van der Aa syndrome (HVDAS), characterised by autism, intellectual disability, and multisystem involvement. The *ADNP* gene is essential for embryonic development and interacts with components of several chromatin remodelling complexes. However, the precise pathophysiological mechanisms underlying the disorder remain incompletely understood.

Methods We used CRISPR/Cas9 genome editing to create a 14-base pair deletion c.2463_2476del (p.Leu822Hisfs*6) in the murine *Adnp* gene to establish a disease-relevant mouse model. Only male mice were used in this study to reduce variability associated with sex-specific differences. Molecular, transcriptomic (RNA-seq), chromatin accessibility (ATAC-seq), proteomic (mass spectrometry), and 3D genome architecture (Hi-C) analyses were performed in cortical brain tissue. Neuroanatomical and behavioural phenotyping, including Morris water maze, elevated plus maze, marble burying, social interaction testing, and the Live Mouse Tracker were conducted to assess cognitive and autism-related phenotypes.

Findings Heterozygous mice are viable and fertile. Introduction of the 14-base pair deletion reduced cellular Adnp levels in the brain ($p = 0.0008$) and decreased its chromatin association ($p = 0.001$), parallelled by a genome-wide increase in chromatin accessibility. Morphological analyses revealed mild neuroanatomical alterations in regions associated with cognition, memory, learning, and motor function ($p < 0.05$). Behavioural testing confirmed cognitive impairment in the Morris water maze ($p < 0.05$), increased anxiety-like behaviour in the elevated plus maze ($p = 0.0035$), repetitive behaviour in the marble burying assay ($p = 0.045$), and impaired social interactions ($p < 0.05$). Transcriptome sequencing of the frontal cortex, an essential region involved in executive functions, cognition, and motor control, revealed predominant downregulation of the Wnt signalling pathway ($p = 0.03$). Cytoskeletal abnormalities were further coupled to synaptic plasticity deficits, dysregulation of transcription

*Corresponding author. Department of Medical Genetics, University of Antwerp, Prins Boudewijnlaan 43/6, 2650 Edegem, Belgium.
E-mail address: claudio.dincal@uantwerpen.be (C.P. D'Incal).

factors implicated in lineage specification, and alterations in neuronal cell numbers. Adnp directly regulated mechanisms of synaptic plasticity through interaction with Camk2a and Dbn1. In heterozygous mice, these protein interactions were disrupted, resulting in aberrant Camk2a phosphorylation at synapses ($p = 0.012$). Mass spectrometry identified changes in multiple chromatin-interacting proteins and cytoskeletal components, corroborating nuclear and cytoskeletal dysregulation observed at the transcriptomic level. Hi-C analysis detected locus-specific alterations in 3D genome architecture associated with transcriptional changes.

Interpretation We generated a disease-relevant heterozygous *Adnp* mouse model that recapitulates key molecular and behavioural features observed in patients with Helsmoortel-Van der Aa syndrome. Our findings demonstrate a role for Adnp in chromatin regulation and Wnt signalling, coupled to aberrant expression of cytoskeletal components and synaptic dysfunction. This mouse model provides a mechanistic framework linking chromatin dysregulation to autism-related behaviours and represents a valuable platform for future preclinical studies.

Funding This work was supported by the Marguerite-Marie Delacroix Foundation (FFP240064 to C.P.D.), the Research Fund of the University of Antwerp (Methusalem grant "GENOMED" to R.F.K.), ERA-NET NEURON ("ADNPinMED"), and the European E-RARE programme ("IMPACT"). Additional support was provided by a crowdfunding initiative from the German ADNP parent community to support C.P.D.; E.P. was supported by the FWO grant G0A1Z24N. C.A.M. received support from the Marguerite-Marie Delacroix fellowship. D.S. was supported by an EMBO fellowship (ALTF 1564-2025). F.P. was supported by a Human Frontier Science Program Long-Term Fellowship (LT000111/2021-L) and an EMBO Long-Term Fellowship (ATLF 716-2020). W.V.B. acknowledges support from the University of Antwerp (ID46420/48076/50799) and COST Action CA18127 (International Nucleosome Consortium 5INC). W.V.B., F.K., E.P., and C.P.D. acknowledge the IMPULS BOF 2024. Infrastructure support was provided by FWO (including IRI grant I000123N, GOH4216N).

Keywords: Helsmoortel-Van der Aa syndrome (HVDAS); Activity-Dependent Neuroprotective Protein (Adnp); Autism; Epigenetics; Chromatin architecture

Research in context

Evidence before this study

Activity-Dependent Neuroprotective Protein (ADNP) is a chromatin-associated factor essential for neocortical neurogenesis. In 2014, our laboratory described a neurodevelopmental syndrome caused by *de novo* heterozygous ADNP variants, now recognised as Helsmoortel-Van der Aa syndrome, characterised by autism spectrum disorder, intellectual disability, language delay, hypotonia, and multisystem involvement. Subsequent genome sequencing initiatives have confirmed the recurrent nature of these variants and their implication in autism spectrum disorder. Complete Adnp loss in mice is embryonically lethal, highlighting its critical role. Haploinsufficient mouse models or mice carrying the p.Tyr718* variant, which mirrors the recurrent human p.Tyr719* variant, have provided important insights into ADNP biology. However, these models do not fully capture variants located in the C-terminal mutational hotspot, have never been made publicly available, and have not been cohesively characterised across the spectrum of human phenotypes, limiting opportunities to investigate disease mechanisms in a patient-relevant context.

Added value of this study

We generated a heterozygous Adnp mouse carrying the c.2463_2476del (p.Leu822Hisfs*6) frameshift variant located in a C-terminal mutational hotspot where recurrent pathogenic variants are observed in humans. Integrated analyses of chromatin accessibility, transcriptomics, proteomics, and behavioural phenotyping demonstrate that this variant disrupts chromatin organisation and transcriptional networks controlling Wnt signalling, cytoskeletal dynamics, and synaptic plasticity, in parallel with behavioural alterations reminiscent of patients. These molecular and functional changes establish a direct link between aberrant ADNP gene function and impaired neurodevelopment.

Implications of all the available evidence

These findings provide a mechanistic framework for Helsmoortel-Van der Aa syndrome, showing how a C-terminal Adnp variant perturbs chromatin, Wnt signalling, and cytoskeletal pathways in male mice. Dysregulated Wnt and cytoskeletal networks represent potential therapeutic targets, and the mouse model offers a translational platform for preclinical testing and further mechanistic exploration of ADNP-related neurodevelopmental disorders.

Introduction

Activity-dependent neuroprotective protein (ADNP) is essential for embryonic development[1] and neocortical neurogenesis.[2] The human *ADNP* gene, located on chromosome 20q13.13, comprises six exons, of which the last three encode the protein.[3] ADNP contains several DNA- and chromatin-binding motifs that mediate its nuclear functions, although some cytoskeletal associations, either direct or indirect, have also been reported.[4] A bipartite nuclear localisation signal (NLS) enables nuclear import.[5] Within the nucleus, ADNP functions as a transcriptional regulator through nine C2H2-type zinc fingers and a homoeobox domain,[6] and is recruited to pericentromeric heterochromatin via a PxVxL and ARKS motif that mediate the interaction with heterochromatin protein 1 (HP1).[7] ADNP forms the core of the ChAHP chromatin remodelling complex together with CHD4 and the HP1 isoforms α and γ[8,9] and recruits WDR5 and HDAC2 to regulate histone and DNA methylation.[10] Beyond its nuclear role, ADNP also interacts with cytoskeletal-associated proteins, including the autophagy mediator LC3,[11] NAD-dependent deacetylase SIRT1,[12] and the synaptic scaffolding protein SHANK3,[13] suggesting additional regulatory features independent of ChAHP.[4]

Heterozygous *de novo* variants in *ADNP* are a recurrent cause of Helsmoortel-Van der Aa syndrome (OMIM, 615873), a neurodevelopmental disorder with autism spectrum disorder (ASD) and intellectual disability (ID).[14,15] A cohort study encompassing 78 patients has defined a characteristic phenotype comprising ASD, mild to severe ID, severe speech and motor delays, and behavioural abnormalities.[16] Additional clinical features include distinctive facial dysmorphisms, short stature, visual impairments, hypotonia, and sleep disturbances.[16,17] Notably, *ADNP* variants exhibit opposing methylation signatures depending on their location within the gene: N-terminal or C-terminal variants are associated with CpG hypomethylation, whereas central variants affecting the NLS sequence display CpG hypermethylation.[18,19] The recurrent p.Tyr719* correlates with delayed motor milestones, suggesting a more severe phenotype compared with other genotypes.[16] Subsequent genotype–phenotype correlations have been refined using facial recognition algorithms, further stratifying patients according to their methylation profiles.[20]

In overexpression systems, wild-type human ADNP localises predominantly to the nucleus,[5,6,10,21] although distribution can vary by cell type and physiological state.[22–24] Experimental modelling of patient-derived variants has revealed profound effects on protein stability and subcellular localisation, allowing classification into three categories: (i) C-terminal variants retain an intact NLS sequence and localise normally to the nucleus with loss of distinct HP1-associated punctate, (ii) variants disrupting the bipartite NLS are mislocalised to the cytoplasm, potentially conferring toxic gain-of-function properties through aberrant protein–protein interactions, and (iii) N-terminal truncating variants result in markedly reduced expression due to proteasomal degradation.[5]

Although multiple mouse models of Helsmoortel-Van der Aa syndrome have been described,[25–28] none of these have been made publicly available. We therefore generated a heterozygous *Adnp* mouse model carrying the engineered c.2463_2476del (p.Leu822Hisfs*6) frameshift variant, positioned near the recurrent human hotspot variants (p.Leu831Ilefs*82 and p.Asn832-Lysfs*81),[16] using CRISPR/Cas9-mediated genome editing. By integrating chromatin accessibility and conformation assays (ATAC-seq and Hi-C), with transcriptomic and proteomic profiling of the frontal cortex, alongside comprehensive behavioural testing, we demonstrate that this variant induces phenotypes characteristic of Helsmoortel-Van der Aa syndrome, including cognitive impairment, anxiety-like behaviour, repetitive activity, and altered sociability. Furthermore, our findings reveal a primary role for Adnp in chromatin regulation and lineage specification, exemplified by suppression of Wnt signalling and concomitant cytoskeletal and synaptic defects leading to impaired neurodevelopment.

Methods

Animals

Adnp heterozygous (HET) mice carrying the c.2463_2476del (p.Leu822Hisfs*6) variant were generated via *in vitro* transcription of single guide RNA (sgRNA) targeting the murine *Adnp* gene (5′-TACAAGCCTGGTGTGCTGCT-3′). Fertilised eggs from C57BL/6JNJcl mice were collected as previously described.[29] The *Adnp* sgRNA (24 ng/μl) was mixed with 100 ng/μl recombinant GeneArt Platinum Cas9 Nuclease (Invitrogen; B25640) in Opti-MEM I (Gibco; 31985062). The mixture was incubated for 10 min at room temperature prior to electroporation, which was performed as described elsewhere.[30]

Following electroporation, embryos were cultured in M16 medium at 37 °C until two-cell stage and then transferred into the oviducts of pseudo pregnant ICR females. Small genomic alterations in the offspring were detected using PCR. The following primers were used: Adnp-Fwd, 5′-GAGTGACATTGCCTCCCATT-3′, and Adnp-Rev, 5′-TTCCCAAGGTTATGCTTTTTG-3′. The resulting PCR products were cloned into a TA-cloning vector (pCR2.1), and Sanger sequencing confirmed the deletion. sgRNA efficiency was assessed by uploading the.abi1 files into the Synthego Inference of CRISPR Edits (ICE) analysis tool.

The resulting C57BL6/6JCr-*Adnp*^{em1Ant}/*Adnp*$^{+}$ mice (RRID:IMSR_JAX:033128) were subsequently backcrossed onto a C57BL/6JCr background. Litters

consisting of wild-type (WT) and HET mice were housed in mixed-genotype groups. Animals were assigned to experimental groups based on genotype only after weaning and genotyping. No additional selection based on phenotype was applied. Mice were housed in standard cages (22.5 cm × 16.7 cm x 14 cm) under controlled temperature and humidity, with a 12 h/12 h light–dark cycle. Food and water were provided *ad libitum*. No additional environmental enrichment was applied to cages. All experiments complied with EU Directive 20120/63/EU (ECD approval code: 2015-83) and were approved by the Animal Ethics Committee of the University of Antwerp.

Randomisation and blinding

Animals were assigned to experimental groups, cages, and testing batches using computer-generated randomisation, stratified by litter where applicable. Experimenters were blinded to genotype during behavioural scoring, histology, and image quantifications. Genotype was revealed only after data acquisition and primary quantification were completed.

Inclusion and exclusion criteria

All offspring were included unless predefined exclusion criteria were met: humane endpoint reached prior to study completion, technical failure (e.g., insufficient RNA integrity, failed library preparation), or failure to meet predefined quality control thresholds for imaging or sequencing. Exclusion criteria were established prior to unblinding and applied uniformly across groups. No post hoc exclusions were performed. Only male mice were included to reduce variability associated with sex-dependent hormonal fluctuations[31,32] and to align with prior studies of Adnp-related neurodevelopmental phenotypes,[26,33] thereby facilitating comparability across datasets.

Unit of analysis

The individual animal was considered the biological unit of analysis. Technical replicates were averaged prior to statistical testing and were not treated as independent observations.

Body weight was measured at 10 weeks of age prior to brain dissection. As data violated assumptions of normality, results are presented as median (IQR) and analysed using a two-sided Wilcoxon rank-sum test.

Adnp mouse genotyping and sequencing

Mice were genotyped with the MyTaq Extract-PCR kit (Bioline; BIO-21127 and BIO-25044) following the manufacturer's instructions. DNA was extracted from tail tissue, and thermocycling was performed with an annealing temperature of 62 °C using the following primers: Adnp-Exon5-Fwd, 5′-AAGGACTCCCGCTT CCATTG-3′ and Adnp-Exon5-Rev, 5′-CAAACAG CCCTATCCCACCA-3′. To exclude potential CRISPR/Cas9 off-target cleavage, the entire coding sequence of the murine *Adnp* gene was amplified and sequenced using additional primers listed in Additional File S1. Amplified products were separated on a 1.5% agarose gel and stained with GelRed Nucleic Acid Gel Stain (Biotium; 41002). The TrackIt 100 bp DNA Ladder (Invitrogen; 10488-058) served as a reference marker. The deletion was confirmed by Sanger sequencing.

Sample size justification and number of animals per experiment

Sample sizes were determined a priori using G*Power (version 3.1) to achieve 80% statistical power at $\alpha = 0.05$. Effect size assumptions (Cohen's $d \geq 0.8$) were based on pilot data and published studies in *Adnp*-related neurodevelopmental mouse models.[25,26,28,33] For high-dimensional or resource-intensive assays (e.g., ATAC-seq, co-immunoprecipitation, and Hi-C), where formal power estimation is less reliable, sample sizes were selected based on established standards to ensure reproducibility while adhering to ethical principles of animal use (Table 1). No interim analyses or post hoc sample size adjustments were performed.

RNA extraction and RT-PCR

Total RNA was extracted from the frontal cortex of WT and HET mice using the RNeasy Mini Kit (Qiagen; 74106) following the manufacturer's protocol. RNA concentration was determined using the Qubit RNA Broad Range Assay Kit (Invitrogen; Q10211). RT-PCR validation of a subset of genes identified in the RNA sequencing experiment was performed by reverse transcribing 1 μg of total RNA into cDNA using the SuperScript III Reverse Transcriptase kit (Invitrogen; 18080093). Primer efficiencies were optimised by standard dilution curve analysis on pooled cDNA from WT and HET mice (90–110% efficiency).

RT-PCR was conducted in technical triplicates that were averaged per biological replicate using the CFX384 Touch Real-Time PCR Detection System (BioRad; 1855484) and the Takyon No ROX SYBR 2× MasterMix (Eurogentec; UF-NSMT-B0701), with primers listed in Additional File S2. Reference gene stability was assessed using the geNorm algorithm in qbase+ (Biogazelle), after which *Actb*, *Gapdh*, and *Rpl13a* were selected for normalisation. Data were analysed in qbase+ (Biogazelle) with a maximum deviation of 0.5 per triplicate. Statistical analysis of RT-PCR quantification was performed within the statistics section described below.

Total protein extraction and subcellular protein fractionation

Murine brain tissue was dissected on ice and immediately snap-frozen in liquid nitrogen. For total protein extraction, whole-brain tissue was homogenised using a TissueRuptor II (Qiagen; 9002755) at low speed in ice-cold RIPA buffer (150 mM NaCl, 50 mM Tris, 0.5%

Experiment	Sample size	Justification for sample size	References
Body weight determination	WT (n = 16), HET (n = 11)	Sample size based on prior phenotyping studies in Adnp deficient and other neurodevelopmental mouse models (10–15 animals per group) sufficient to detect medium effect sizes (Cohen's d $\geq$ 0.8) in body weight and morphological outcomes with 80% power (α = 0.05) as determined by G*Power.	34
Western blotting	WT (n = 4), HET (n = 4)	Western blot experiments were used to validate protein-level differences identified in omics analyses. This sample size is commonly employed for biochemical validation and provides adequate detection of large effect sizes (α = 0.05).	34
Histomorphological phenotyping and	WT (n = 5), HET (n = 5)	Group sizes were chosen based on prior neuroanatomical phenotyping studies, providing sufficient power to detect region-specific morphological differences with moderate-to-large effect sizes while minimising animal use.	35–37
Behavioural test battery	Cohort 1: WT (n = 19), HET (n = 12) Cohort 2: WT (n = 16), HET (n = 15) For LMT specifically: WT (n = 17), HET (n = 14)	Behavioural phenotyping studies commonly include $\geq$12 animals per genotype to detect moderate behavioural differences. Sample sizes were determined using G*Power for 80% power (α = 0.05) and confirmed across two independent cohorts for reproducibility.	34,38–41
RNA sequencing	WT (n = 7), HET (n = 7)	Sample size (n = 7/group) provides sufficient statistical power (>80%) to detect $\log_2$FC $\geq$ 0.5 with FDR <0.05, consistent with prior RNA-seq power analyses and confirmed using G*Power (α = 0.05).	42
Immunostainings (of neurons, astrocytes, and microglia)	WT (n = 8), HET (n = 6) A minimum of 5 animals per genotype was used	Group sizes determined a priori with G*Power (80% power, α = 0.05) to detect 20–30% genotype differences in cortical cell counts, consistent with prior immunohistochemical quantification studies.	43
Co-immunoprecipitation (CoIP)	WT (n = 2), HET (n = 2)	CoIP validation experiments aim to confirm protein–protein interactions rather than perform statistical hypothesis testing. Two independent biological replicates are standard for reproducibility in mechanistic assays.	12,13,44,45
Synaptoneurosome preparation and stimulation	WT unstimulated (n = 5) HET unstimulated (n = 6) WT L-glutamate (n = 5) HET L-glutamate (n = 5)	Exploratory biochemical validation assay conducted on independent cortical preparations. Group sizes align with prior synaptoneurosome protocols focussing on mechanistic reproducibility rather than power-based inference.	45,46
Label-Free Quantitative Proteomics (LFQ-MS)	WT (n = 7), HET (n = 7)	The same animals used for RNA sequencing were re-used for proteomic profiling, providing matched transcriptomic-proteomic comparison and equivalent statistical power (80% power, α = 0.05) as determined in RNA-seq sample size estimation.	47–49
Hi-C/ATAC-seq library construction and processing	WT (n = 2), HET (n = 2)	Hi-C and ATAC-seq are high-cost, genome-wide chromatin sequencing assays. Two biological replicates per genotype are standard in the field to ensure reproducibility, as established in ENCODE and other reference studies.	9,50,51

Sample sizes were determined using G*Power (version 3.1) for 80% power at α = 0.05, unless stated otherwise.

Table 1: **Sample size and justification for each experimental procedure.**

sodium deoxycholate, 1% NP-40 and 2% sodium dodecyl sulphate), supplemented with the cOmplete, Mini, EDTA-free Protease Inhibitor Cocktail (Roche; 04693159001) together with PhosSTOP phosphatase inhibitor (Roche; 4906845001). Lysis was carried out for 1 h at 4 °C with agitation, and cell debris was removed by centrifugation for 30 min at maximum speed in a pre-cooled centrifuge.

For subcellular fractionation, 200 mg of whole-brain tissue was homogenised using a pestle and mortar and sequentially fractionated into cytoplasmatic, membrane-bound, nuclear-soluble, chromatin-bound, and cytoskeletal protein fractions using the Subcellular Protein Fractionation Kit for Tissues (Thermo Scientific; 87790) following the manufacturer's instructions. Purity of the enriched protein fractions was verified by Western blot analysis using fraction-specific marker proteins. Protein concentrations were determined using the Pierce BCA Protein Assay Kit (Thermo Scientific; 23225).

Antibodies

All antibodies used in this study are listed in the reagent validation file (Additional File S3), including supplier, catalogue number, host species, reactivity, immunogen, optimised dilution, and research resource identifiers (RRID) tags. Only commercial antibodies were used and were selected based on prior validation for the indicated applications and expected molecular weight of the target protein. Antibody specificity was confirmed in our experimental system by detection of bands at the expected molecular weight. For Adnp, specificity was further supported by the absence or marked reduction of signal in knockout cell lines and by blocking peptide competition assays, as previously reported.[52] All antibodies were optimised prior to experimental use by performing dilution series to determine the linear range of detection and to confirm proportional signal response to protein input.

Western blotting

A total amount of 20 µg protein lysate was reduced with NuPAGE Sample Reducing Agent (Invitrogen; NP0009) in NuPAGE LDS Sample Buffer (Invitrogen; NP0007). Samples were heated for 10 min at 70 °C and separated using a Bolt 4–12%, Bis-Tris, 1.0 mm, Mini Protein Gels (Invitrogen; NW04120BOX) using Bolt MOPS SDS Running Buffer (Invitrogen; B0001). Proteins were

then transferred onto Amersham Protran Premium nitrocellulose membranes (Cytiva; GE10600008) using a Mini Trans-Blot cell (Biorad; 1703930) with a transfer buffer (25 mM Tris, 192 mM glycine, and 20% methanol). Successful transfer was verified by staining with Ponceau S solution (Sigma Aldrich; P7170).

Membranes were blocked for 1 h at room temperature with agitation in either 5% blocking-grade non-fat dry milk (NFDM) (Carl Roth; T145.4) or 5% bovine serum albumin (BSA) (Carl Roth; CP84.1) dissolved in tris-buffered saline with Tween-20 (TBST). Primary antibodies were optimised within a 1:1000–1:5000 dilution range in either 5% NFDM/TBST or 5% BSA/TBST. Signal amplification was achieved with appropriate HRP-conjugated secondary antibodies (RRID:AB_2617138 and RRID:AB_2636929) in a 1:2000 dilution. Chemiluminescent detection was performed using SuperSignal West Pico PLUS Chemiluminescent Substrate (Thermo Scientific; 34580) and for ADNP-specific detection, West Femto Maximum Sensitivity Substrate (Thermo Scientific; 34095) was used.[52]

Images were captured using the Amersham Imager 680 (Cytiva). Gapdh served as a loading control for total protein extracts. For subcellular fractionations, Gapdh (RRID: AB_561053) was used for cytoplasmic proteins, E-cadherin (RRID: AB_397580) for membrane-bound proteins, PPARα (RRID: AB_448110) for nuclear proteins, histone H3 (RRID: AB_470239) for chromatin-bound proteins, and β-actin (RRID: AB_476744) for cytoskeletal proteins. Image quantification was performed using ImageJ software. Band intensities were normalised to loading controls and averaged across biological replicated prior to analysis. Statistical analysis of Western blot quantification was performed within the statistics section described below. Uncropped full blots with labelling and loading controls are provided in the Supplemental Western blots File.

ATAC sequencing and data analysis

Frozen mouse cortical tissues were received at Azenta (GENEWIZ, LLC.; South Plainfield, NJ, USA) on dry ice and stored in liquid nitrogen upon receipt until further processing. Intact nuclei were extracted using the Miltenyi Nuclei Extraction Buffer (Miltenyi Biotec, Auburn, CA, USA) following manufacturer's protocol, with gentle MACS dissociation using C tubes. Following isolation, nuclei were counted using acridine orange/propidium iodide (AO/PI) dye on the Nexcelom Cellaca MX.

ATAC-seq library preparation and sequencing were performed at GENEWIZ, LLC. (South Plainfield, NJ, USA). Thawed live-cell samples were washed and treated with DNase I (Life Tech; EN0521) to remove genomic DNA contamination. Cell viability and concentration were assessed using a Countess Automated Cell Counter (ThermoFisher Scientific, Waltham, MA, USA). After cell lysis and cytosol removal, nuclei were treated with Tn5 transposase (Illumina; 20034197) for 30 min at 37 °C and purified using the Minelute PCR Purification Kit (Qiagen; 28004) to yield tagmented DNA.

Tagmented DNA was barcoded with the Nextera Index Kit v2 (Illumina; FC-131-2001) and amplified by PCR prior to SPRI bead cleanup to produce purified DNA libraries. The sequencing libraries were validated using the Agilent TapeStation (Agilent Technologies, Palo Alto, CA, USA), and quantified by using Qubit 4.0 Fluorometer (Invitrogen, Carlsbad, CA), as well as by quantitative PCR (KAPA Biosystems, Wilmington, MA, USA). Illumina reagents and kits were used for cluster generation and sequencing. Libraries were multiplexed on a flow cell and loaded onto the Illumina NovaSeq instrument following the manufacturer's instructions. Sequencing was carried out using a 2 × 150 bp paired-end configuration.

Image analysis and base calling was conducted by the NovaSeq Control Software (NCS) v1.8.1. Raw sequencing data (.bcl files) were converted into.fastq files and de-multiplexed using Illumina's bcl2fastq 2.20 software, allowing one mismatch for index sequence identification.

ATAC-seq sequencing reads were aligned to the mm10 mouse genome using bowtie2 v.2.4.4 command: "*bowtie2-p12–no-mixed–no-discordant*").[53] Low-quality reads were filtered with SAMtools v.1.9 command: "*samtools view* -b -q 30"),[54] and BAM files were sorted, deduplicated, and indexed using Sambamba v1.0 command: "*sambamba sort*"; "*sambamba markdup –remove-duplicates*") with default parameters.[55] Normalisation factors were generated by creating a count matrix over 10 kb genomic bins using the *featureCounts* function of the Subread package, followed by TMM normalisation using the edgeR package. BigWig files were created using deepTools command: "*bamCoverage –scaleFactor norm.factor*"),[56] and tracks were visualised in IGV v.2.16.1.[57] ATAC-seq peaks were called on each replicate using MACS3 with a q-value cutoff of 0.05.[58] Heatmaps and metaplots were produced using the *computeMatrix* function and visualised with the *plotHeatmap* and *plotProfile* functions.

Histomorphological phenotyping of adolescent Adnp heterozygous mouse brains

Neuroanatomical analyses were performed on male WT and HET mice at the age of 10 weeks. Standard operating procedures are described in detail elsewhere.[35,37] Briefly, mice were sacrificed by cervical dislocation prior to brain dissection. Whole brains were fixed in 10% buffered formalin for 48 h and then transferred to 70% ethanol. Samples were embedded in paraffin and sectioned at 5 µm thickness using a microtome (Leica RM 2145) to obtain sagittal brain slices at lateral coordinate +0.60 mm.

Sections were stained with 0.1% Luxol fast blue (Sigma Aldrich; *L0294*) and 0.1% Cresyl Violet acetate

(Sigma Aldrich; *C5042*) and scanned at single-cell resolution using Nanozoomer whole-slide scanner 2.0HT, C9600 series (Hamamatsu Photonics, Shizuoka, Japan).

For sagittal sections, 22 neuroanatomical structures were quantified at lateral coordinate +0.6 mm based on area, length, and cell-level features: (1) total brain area; (2) primary and secondary motor cortices; (3) pons; (4) cerebellar area, the internal granular layer, and medial cerebellar nucleus; (5) lateral ventricle; (6) corpus callosum; (7) thalamus; (8) caudate putamen; (9) hippocampus and associated layers; (10) fimbria of the hippocampus; (11) anterior commissure; (12) stria medullaris; (13) fornix; (14) optic chiasm; (15) hypothalamus; (16) pontine nuclei; (17) substantia nigra; (18) the fibres of the pons; (19) cingulate cortex; (20) dorsal subiculum; (21) inferior colliculus; and (22) superior colliculus.

Measurements were performed blinded across three sagittal sections per animal. All samples were systematically assessed for cellular ectopia (misplaced neurons) and scored based on four parameters: (1) suitability for analysis, (2) staining intensity and contrast, (3) symmetry, and (4) sectioning precision. Each section was verified against stereotaxic coordinates from the Mouse Brain Atlas. Statistical analysis was performed as described in the statistics section.

Immunohistochemistry of frozen brain sections (IHC-Fr)

Male WT and HET mice, aged 10 weeks, were used for immunohistochemistry. Animals were humanely killed by intraperitoneal injection of sodium pentobarbital (133.3 mg Dolethal/kg body weight). Whole brains were removed, and hemispheres were separated. Tissues were fixed in 4% formaldehyde (ROTIHistofix, Carl Roth; *3105.2*) for 2 h at room temperature, washed in PBS (0.01 M; pH 7.4), and cryoprotected in 20% sucrose/PBS overnight at 4 °C.

Samples were embedded in PELCO Cryo-Embedding Compound (Ted Pella, Inc.; *27300*) and stored at –80 °C. Cryosections (10 µm) were cut using a Leica CM1950 Cryostat (Leica Biosystems, Wetzlar, Germany) and mounted on VWR SuperFrost Plus, Adhesion Slides (VWR; *631-0108*). Sections were washed three times in PBS, then blocked, and permeabilized in PBS containing 0.05% thimerosal, 0.01% NaN_3, 0.1% BSA, 1% Triton X-100, and 10% normal horse serum. Sections were incubated overnight at room temperature with primary Adnp antibody (RRID: AB_3097704) in blocking/permeabilization buffer. After six PBS washes, sections were incubated for 4 h with Cy3-conjugated Fab fragment donkey anti-rabbit secondary antibody (RRID: AB_2340606) in PBS containing 0.05% thimerosal, 0.01% NaN3, 0.1% BSA, and 10% normal horse serum. Following six washes, nuclei were counterstained with 5 µg/mL DAPI for 5 min and washed three washes in PBS. Immunostained cryosections were mounted in Citifluor AF1 Mountant Solution (Electron Microscopy Sciences; *17970-100*).

Confocal images were acquired using a Leica SP8 scanning confocal microscope (Leica-microsystems, Wetzlar, Germany) equipped with a 405 nm diode laser (for DAPI) and the DPSS 561 nm laser (for Cy3). Three independent cryosections per mouse were analysed, with two images acquired per region (hippocampus, cortex, and cerebellum). Images were captured using a 20× objective (HC PL APO 20×/0.75 IMM CORR CS2) and analysed in FIJI (ImageJ).[59] Nuclei were identified as DAPI + regions following automated thresholding (Huang method) of the smoothed DAPI channel (Gaussian blur, kernel size 2). Mean Adnp intensity was measured within DAPI + regions and averaged per animal and brain region. Statistical analysis of frozen immunosections was performed as described in the statistics section.

Behavioural test battery

Two independent cohorts of male adolescent WT and HET mice were tested at 10 weeks of age using a standardised behavioural test battery assessing cognitive, motor, repetitive, and social behaviours. Animals were randomly assigned to testing batches, and all behavioural scoring was performed blinded to genotype. Behavioural assays were performed in a predefined order identical across cohorts. For repeated-measures designs (e.g., Morris Water Maze), repeated-measures ANOVA was used with time as a within-subject factor. For group-housed behavioural data, linear-mixed effect models were applied with genotype as a fixed effect and cage as a random effect to account for clustering. Detailed statistical analysis was performed as described in the statistics section.

Morris Water Maze (MWM)

Hippocampus-dependent spatial learning and memory were evaluated using the MWM test as described previously.[60] The circular pool (diameter 150 cm, height 30 cm) was filled with opaque water (25 °C) using non-toxic white paint, and distal visual cues were placed around the pool. The hidden platform (diameter 15 cm) was submerged 1 cm below the surface in a fixed quadrant. The acquisition phase consisted of four consecutive days, each containing two daily blocks (10:30 AM and 03:00 PM) of four trials with a 15-min intertrial interval. Each trial lasted 120 s, and mice that failed to locate the platform were guided to it and allowed to remain for 10 s. A probe trial was performed four days after the acquisition phase, during which the platform was removed, and trajectories were recorded for 100 s using the EthoVision XT (Noldus, The Netherlands). Performance measures included path length, escape latency, and swim speed during acquisition and percentage time spent and entries in each quadrant during probe trial.

Passive avoidance

Aversive learning and memory were assessed using a step-through passive avoidance task.[38] The apparatus consisted of an illuminated compartment connected to a dark compartment by a sliding door. Mice were placed in the lit chamber, and after 5 s the door was opened. Upon full entry into the dark compartment (four paws), mice received a mild foot shock (0.3 mA for 1 s). After 24 h, the latency to re-enter the dark compartment was recorded for up to 300 s.

Accelerating rotarod

Motor coordination and balance were tested using an accelerating rotarod apparatus (Panlab, Barcelona, Spain).[38] After two acclimatation trials at a constant speed (4 rpm, 2 min), mice underwent 4 test trials with the rod accelerating from 4 to 40 rpm. The latency to fall was recorded with a 5-min cut-off.

Elevated plus maze

Anxiety-like behaviour was evaluated using the elevate plus maze.[39] The apparatus consisted of two opposing arms, and two closed arms (30 cm × 5 cm) elevated 60 cm above the floor. Mice were placed in the central area facing a closed arm and allowed to explore for 5 min. Trajectories were recorded using EthoVision XT (Noldus, The Netherlands).

Marble burying test

Repetitive behaviour was assessed during the dark phase using the marble burying assay. Mice were habituated individually for 30 min in experimental cages (22.5 × 16.7 × 14 cm), containing 5 cm of bedding (Grade 5, Brandenburg). Twenty dark blue glass marbles (13 mm in diameter) were arranged in a 4 × 5 grid on the bedding surface. Mice were allowed to explore for 30 min, after which the number of marbles buried (>2/3 covered) were counted.

Social exploration test

Social approach behaviour was evaluated as described previously.[39] The apparatus consisted of a 50 × 50 cm open arena with a circular enclosure in the centre housing a stimulus mouse (WT male or female C57BL/6JCr, Charles River, France. Test mice were placed in a corner of the arena and recorded for 10 min following a 1-min habituation period. Trajectories and zone entries were tracked using EthoVision XT (Noldus, The Netherlands).

Three–chamber test for sociability and social novelty

Sociability and preference for social novelty were assessed in a three-chamber apparatus (20 × 40 × 47 cm).[60] Each trial was video recorded using EthoVision XT (Noldus, The Netherlands). After a 5-min habituation to the central chamber, mice explored all three chambers for 10 min. During the sociability phase, a stranger mouse (WT male, mouse 1) was enclosed under a wire cup in one side chamber, and an identical empty cup (object) was placed in the opposite chamber. Following a 10- minute test, mice were returned to the central chamber. During the social novelty phase, a novel stranger mouse (WT male, mouse 2) replaced the empty cup, while the familiar mouse 1 remained. Time spent near each cup and locomotion patterns were recorded. Chamber location of stimulus mice were counterbalanced across trials.

Live Mouse Tracker (LMT)

Group and social behaviours were continuously monitored using the LMT system.[40] The setup consisted of a Plexiglas cage (50 × 50 cm) equipped with 16 radio frequency identification (RFID) antenna coils and an infrared depth camera. RFID tags (Biomark 12.5 mm) were subcutaneously injected two weeks prior to the LMT recordings. Groups of three or four littermates were recorded for 24 h without disturbance under controlled environmental conditions (08:00 AM–08:00 PM light/dark cycle). Male adolescent mice were tested over nine different LMT recordings. Behavioural events were automatically extracted using the open-source LMT framework (livemousetracker.org) and included 33 individual behavioural events of one single mouse, such as head down, stop, rearing, jump, SAP (stretched attend posture), move alone, stop alone and rear isolated. On the other hand, social behavioural events between two, three, or four mice were recorded, such as move in contact, rear in contact, contact, stop in contact, contact side–side, contact side–side opposite, contact nose–nose, contact nose-anogenital, group forming of two, group forming of three, train of two, train of three, follow, social approach, approach from the front, approach from the rear, make contact, make a group of three, make a group of four, get away, break contact, break a group of three, break a group of four, sequences of oral–oral—oral-genital contact and sequences of oral-genital—oral–oral contact.

RNA sequencing and data analysis

Total RNA was extracted from the frontal cortex of WT and HET mice described above. Samples with the highest RNA integrity number (RIN) score (RIN > 6.5) were selected for bulk RNA-seq, which was performed by Novogene (Cambridge, UK). Library preparation was conducted using the Novogene NGS RNA Library Prep Set (PT042), and sequencing was carried out on the Illumina Novaseq 6000 platform using a paired-end 150 bp (PE150) strategy.

Raw sequencing reads were processed with trimmomatic to remove adaptor sequences and low-quality reads. Clean reads were aligned to the *Mus musculus* reference genome (GRCm38.p6, Ensembl v102) using STAR. Gene-level quantification was performed using featureCounts (Subread package).[61] Differential expression analysis was

performed using DESeq2 in RStudio. Genes with a Benjamini-Hochberg false discovery rate (FDR)-adjusted p-value <0.05 and an absolute $\log_2$FC ($|\log_2 FC| \geq 0.5$ were considered statistically differentially expressed and included in downstream analyses.

Functional enrichment analyses (fGSEA) of differentially expressed genes (DEGs) were performed, and visualisation was supported by the BigOmics analytic platform, an interactive web-based tool for transcriptomic data interpretation.[62] A subset of 20 DEGs was validated by RT-PCR using primers listed in Additional File S2. Transcriptional regulatory network analysis was conducted using the iRegulon plugin in Cytoscape, which identified transcription factors, their putative targets, and the enriched motifs of tracks associated with co-expression patterns among upregulated and downregulated genes.

Immunostaining of neurons, astrocytes, and microglia

Male WT and HET mice, aged 10 weeks, were used. Frozen brain sections were prepared as described above. Sagittal cryosections (70 µm thickness) were generated using a Leica CM1950 Cryostat Microtome (Leica Biosystems, Wetzlar, Germany) and mounted on VWR SuperFrost Plus, Adhesion Slides (VWR; *631-0108*). Sections were washed three times with PBS containing 0.1% Triton X-100 and permeabilized in PBS, containing 0.25% Triton X-100. Blocking was performed for 1 h at room temperature in PBS containing 10% donkey serum, 0.25% Triton X-100, and 2% BSA. Sections were then incubated overnight at 4 °C with primary antibodies diluted in blocking buffer: NeuN (RRID: AB_2341095) for neurons, Iba1 (RRID: AB_839504) for microglia, and GFAP (RRID: AB_304558) for astrocytes. After three PBS washes containing 0.1% Triton X-100, sections were incubated for 90 min at room temperature with appropriate secondary antibodies (RRID:AB_2536183, RRID:AB_2921070, and RRID:AB_2534117) diluted in blocking buffer. Nuclei were stained with Hoechst Nucleic Acid Stain (Invitrogen; H3570) for 10 min in a 1:10,000 dilution followed by two PBS washes. Stained cryosections were transferred to a 0.2% gelatine solution (Sigma–Aldrich; G6144) and mounted using Glycergel mounting medium (Morphisto; 13553.00100). Images were captured using a Nikon Ti2 Automated Spinning Disk microscope (Nikon Instruments Inc., Tokyo, Japan) with a 20× objective Plan APO λD 20× OFN25 DIC N2 objective. For each condition, 3–4 randomly selected fields were imaged from the cortex, hippocampus, and cerebellum. The cortical regions further analysed included the motor, somatosensory, and visual cortices. Image quantification was performed in QuPath v0.5.1 (https://qupath.github.io). For NeuN and Iba1 quantification, Hoechst-positive nuclei were detected, and NeuN + or Iba1+ cells were counted to calculate number of positive cells per mm^2. GFAP quantification was based on the proportion of GFAP + area (GFAP + area/region of interest x 100). Regions of interest (ROI) were manually delineated in QuPath for each slice. Statistical analysis was performed as described in the statistics section.

Co-Immunoprecipitation (CoIP) of synaptic plasticity regulators

Protein–protein interaction networks between Adnp and DEGs enriched for synaptic plasticity were predicted using the STRING database (version 12.0). Expression of the candidate regulators was verified by *in situ* hybridisation using antisense RNA probes targeting the genes of interest. Sagittal sections from postnatal day 28 (P28) male C57BL/6J brains were accessed from the Allen Mouse Brain Atlas (https://mouse.brain-map.org/).

CoIP was performed as previously described.[10,12] Briefly, proteins were extracted from frontal cortical lysates enriched for cytoplasmic and cytoskeletal fractions (see above) from WT and HET mice at 10 weeks of age using the Pierce Co-Immunoprecipitation Kit (Thermo Scientific; 26149). Here, 10 µg of the IP-competent C-terminal Adnp antibody (RRID: AB_3097704) was crosslinked to 50 µL of AminoLink Plus Coupling Resin. An amount of 1 mg of protein lysate was incubated overnight at 4 °C on an end-over-end shaker (VWR; 444–0503). Proteins were eluted in 50 µL of 4× Laemmli Sample Buffer (Biorad; 1610747) supplemented with 10× NuPAGE Sample Reducing Agent (Invitrogen; NP0004). Input, flow-through, and eluted fractions (40 µg each) were loaded on the SDS-PAGE gels and immunoblotted with primary antibodies: anti-Adnp (RRID: AB_3097704), anti-Dbn1 (RRID: AB_3069439), and anti-Camk2a (RRID: AB_2070308). Proteins were visualised using SuperSignal West Femto Maximum Sensitivity Substrate (Thermo Scientific; 34094) following incubation with appropriate secondary antibodies (Agilent). Band intensities of eluted samples were quantified in ImageJ and normalised to the corresponding Adnp input signals. Due to the limited sample size, no formal statistical testing was performed. Data were presented descriptively.

Motif analysis of murine Adnp (UniProt; Q9Z103), Dbn1 (UniProt; Q9QXS6), and Camk2a (UniProt; P11798) was performed using the Eukaryotic Linear Motif (ELM) database (http://elm.eu.org), with p-values determined using amino acid frequency-based probability filters. Three-dimensional protein models were generated with AlphaFold (https://alphafold.ebi.ac.uk) and used for docking analysis on ClusPro2.0 (https://cluspro.org). The top 10 predicted complexes were superimposed in UCFS ChimeraX v1.6.1. to visualise probable binding interaction.

Synaptoneurosome preparation and stimulation

Synaptoneurosomes were purified from the frontal cortex of 10-week-old WT and HET mice, following

established protocols.[46] Frontal cortices were dissected on ice, washed in ice-cold PBS, and homogenised in buffer containing 0.32 M sucrose, 1 mM EDTA, 1 mg/mL BSA, and 5 mM HEPES (pH 7.4) using a Potter-Elvehjem homogeniser. Homogenates were centrifuged at 3000 × *g* for 10 min at 4 °C, and supernatants were recentrifuged at 14,000 × *g* for 10 min at 4 °C. Pellets were resuspended in Krebs–Ringer buffer (140 mM NaCl, 5 mM KCl, 5 mM glucose, 1 mM EDTA, and 10 mM HEPES pH 7.4) and mixed with one volume of 45% v/v Percoll. After centrifugation at 14,000 × *g* for 2 min at 4 °C, the enriched synaptoneurosomal layer was collected, washed, and resuspended in Krebs-HEPES buffer (147 mM NaCl, 3 mM KCl, 10 mM glucose, 2 mM $MgSO_4$, 2 mM $CaCl_2$, and 20 mM HEPES pH 7.4).

Synaptoneurosomes were stimulated in Krebs-HEPES buffer at 37 °C with 100 μM L-glutamate (Abcam; ab120049) for 30 s, 1 min, or 5 min. Following stimulation, samples were centrifuged for 30 s at 14,000 × *g* at 4 °C. Proteins were extracted in ice-cold RIPA buffer containing 2% SDS (see above), and 10 μg of total protein was analysed by SDS-PAGE and Western blotting to probe for Camk2a (RRID: AB_2070308) and phospho-Thr286 Camk2a (RRID: AB_2713889). Ponceau Red solution served as a loading control for total protein abundance.

Band intensities were quantified using ImageJ according to standard procedures. To account for minor variability in total protein content between replicates, phosphorylated Camk2a levels were normalised to total Camk2a (Ponceau Red-normalised phospho-Camk2a divided by Ponceau Red-normalised total Camk2a). Analysis of synaptosome responses were performed as described in the statistics section.

Label-free quantification proteomics (LFQ-MS) and data processing

Total protein was extracted from the frontal cortex from WT and HET mice using ice-cold RIPA buffer (150 mM NaCl, 50 mM Tris, 0.5% sodium deoxycholate, 1% NP-40 and 5% sodium dodecyl sulphate), supplemented with the cOmplete, Mini, EDTA-free Protease Inhibitor Cocktail (Roche; 04693159001) together with PhosSTOP phosphatase inhibitor (Roche; 4906845001). Tissue homogenisation was performed with the TissueLyser II bead homogeniser (Qiagen; 85300). Lysates were incubated for 30 min at 4 °C with agitation, and insoluble debris was removed by centrifugation at maximum speed for 30 min in a precooled centrifuge. For digestion, 15 μg of total protein was reduced, alkylated, and digested with Trypsin Gold, Mass Spectrometry Grade (Promega; *V5280*) using the S-Trap micro kit (ProtiFi; K02-Micro-10), according to the manufacturer's protocol.

Nano-liquid chromatography (nLC) was performed on a Dionex ULTIMATE 3000 system coupled online to a Q Exactive Plus Hybrid Quadrupole-Orbitrap Mass Spectrometer (Thermo Scientific, Massachusetts, USA). Peptides were loaded in five technical replicates onto a 75 μm × 150 mm, 2 μm fused silica C18 capillary column and eluted with buffer A (0.1% formic acid in Milli-Q water) and buffer B (0.1% formic acid in 80% acetonitrile/Milli-Q water). A linear gradient from 5% to 95% buffer B was applied over 120 min at 0.3 μL/min. The MS operated in positive ion mode with data-dependent acquisition. Full MS1 scans were acquired from m/z 375–2000 at 140,000 resolutions, followed by MS2 acquisition at 17,500 resolutions after peptide fragmentation (NCE = 28 eV).

Raw files (*.RAW) were processed in PEAKS AB 2.0 (Bioinformatics Solutions Inc.) using target-decoy search against the murine UniProt database (FDR = 1%). Trypsin was set as the protease (maximum two miscleavages), carbamidomethylation as a fixed modification, and label-free quantification (LFQ) with "match between runs" enabled. Intensity data were imported into MetaboAnalyst 6.0 (https://www.metaboanalyst.ca/MetaboAnalyst/home.xhtml), quantile normalised, log-transformed, and autoscaled. Statistical analysis was performed as described in the statistics section.

Selected proteins were validated by Western blotting (described above). Band intensities were quantified using ImageJ and normalised to Gapdh (RRID: AB_561053). Significantly regulated protein IDs were submitted to MetaScape for pathway enrichment[63] and STRING version 12.0 for protein–protein interaction network analysis.

Hi-C library construction and processing

Crosslinked nuclei were isolated from the frontal cortex of WT and HET mice as previously described[64] and flash-frozen in aliquots of 750,000 nuclei. Hi-C libraries were generated using the EpiTect Hi-C kit (Qiagen; 59971) with the following modifications: chromatin digestion for 4 h, end labelling for 1 h, and proximity ligation for 4 h. Amplified libraries were pooled equimolarly and sequenced at a total depth of 3 billion paired end 100 bp reads. FASTQ files were processed using HiC-Pro v3.1.0[65] Bowtie2 v2.4.4, aligned to the mm10 reference genome. Singleton, multi-hit, and duplicate reads were removed. Read pairs were assigned to GATC restriction fragments, excluding invalid pairs. Contact matrices at 1 kb resolution were generated using the cooler library,[66] and converted into multiresolution matrices for visualisation in HiGlass.[67] Reproducibility of uncorrected matrices was evaluated at 10 kb resolution using HiCExplorer.[68] Genome-wide eigenvector decomposition, insulation score calculation, as well as P-curve, compartment, and insulation profiles generation were performed with cooltools.[69] Loop calling was executed at 10 kb resolution using Moustache with default parameters.[70] Aggregate loop

analyses were conducted using Coolpuppy, normalised by random shifts (n = 10).[71] Publicly available ChIP-seq datasets were integrated for comparison: Adnp from mouse embryonic stem cells (GEO accession number GSE97945) and CTCF from adult mouse whole brain (GEO accession number GSM1446329). Peaks were called using MACS3,[58] and k-means clustering (k = 4) of Adnp and CTCF peaks was visualised using deeptools.[56]

Statistics

All statistical analyses were performed using R (version 4.3.1) and GraphPad Prism (version 9.3.1). All tests were two-tailed.

General analytic framework

Normality was assessed using the Shapiro–Wilk test, and homogeneity of variances was evaluated using the Brown–Forsythe test. Where assumptions of normality and homoscedasticity were satisfied, parametric tests were applied. Otherwise, appropriate non-parametric alternatives were used. For comparisons between two independent groups, unpaired two-tailed Student's t-tests were used for parametric data, and Wilcoxon rank-sum tests for non-parametric data. For experiments involving more than two groups or multiple factors, one-way or two-way ANOVA was applied as appropriate. When repeated measurements were collected across time or conditions, repeated-measures ANOVA was used with Geisser-Greenhouse correction when sphericity was violated. Significant main effects or interactions were followed by post hoc tests using Tukey's or Šidák's multiple comparisons tests, as appropriate to experimental design. Effect sizes and 95% confidence intervals were reported where appropriate.

Hierarchical and clustered data

Behavioural datasets with hierarchical or longitudinal structure (including group-housed animals or repeated observations per cage) were analysed using linear mixed-effects models (LMMs), with genotype treated as a fixed effect and cage identity as a random intercept to account for within-cage clustering. Where applicable, within-cage normalisation was used to reduce batch or housing effects, and model assumptions were verified through residual diagnostics.

High-dimension omics data

Statistical analyses for omics datasets were conducted using established pipelines, with interference performed on processed data outputs as follows. RNA sequencing: differential expression analysis was performed using DESeq2. P-values were adjusted for multiple testing using the Benjamini-Hochberg false discovery rate (FDR), with significance defined as FDR <0.05. Gene set enrichment analyses were performed using GSEA and fast GSEA (fGSEA), with FDR correction applied to pathway-level results. Proteomics (LFQ-MS): protein abundance differences were assessed using two-sided t-tests as implemented in the respective analysis pipeline, followed by FDR correction ($q < 0.05$). ATAC sequencing: data were processed using MACS2 peak calling, followed by differential accessibility analysis based on normalised signal intensities and appropriate statistical testing consistent with distributional assumptions. Genome-wide accessibility changes were interpreted alongside replicate concordance metrics and quality control summaries. Hi-C: data were analysed using normalised contact matrices. Statistical comparisons of insulation scores, loop intensities, compartment strength, and TAD-related features were performed using appropriate parametric or non-parametric tests as above, with emphasis on replicate concordance and genome-wide structure stability. Locus-specific analyses were interpreted in the context of multiple testing and biological replication.

Targeted validation experiments

For RT-PCR, Western blot, immunostaining and image-based quantification, statistical testing followed the general framework above (parametric or non-parametric-based on distributional assessment). When multiple comparisons were performed within a single experimental framework, FDR or Benjamini-Hochberg correction was applied as specified above. For imaging-based quantifications, analyses were performed blinded to genotype.

Data presentation

Data are presented as mean ± standard deviation (s.d.) for parametric analyses and as median with interquartile range (IQR) for non-parametric analyses. Statistical significance was defined as $p < 0.05$ for classical analyses or FDR-adjusted $q < 0.05$ for high-dimension omics datasets. All statistical analyses were performed on biologically independent samples. Technical replicates were not treated as independent observations unless explicitly stated. Statistical methods were applied consistently across experimental modules to ensure comparability or inference.

Ethics statement

All experimental procedures involving mice were approved by the University of Antwerp Animal Ethics Committee (ECD code 2015-83) and conducted in full accordance with the EU Directive 2010/63/EU on the protection of animals used for scientific purposes. All efforts were made to minimise animal suffering and to reduce the number of animals used, in line with the principles of the 3 Rs (Replacement, Reduction, Refinement). This study is reported in accordance with the ARRIVE guidelines.

Role of funders

The funders had no role in study design, data collection, data analysis, data interpretation, or writing of the manuscript.

Results

Heterozygous Adnp mice exhibit reduced expression and chromatin alterations in the brain

We used CRISPR/Cas9-mediated genome editing in mouse oocytes to generate a 14-bp deletion introducing a premature termination codon in the final coding exon of the murine *Adnp* gene, a region located just upstream of a mutational hotspot identified in Helsmoortel-Van der Aa syndrome patients[16] (Fig. 1A). To exclude off-target effects, Sanger sequencing of all *Adnp* coding exons confirmed an exclusive heterozygous 14-bp deletion in exon 6, resulting in the p.Leu822Hisfs*6 frameshift variant located in the heterochromatin protein 1 (HP1)-interacting PxVxL motif (Fig. 1B–E). The sequencing trace files (.ab1) from WT and HET mice were analysed using the Synthego ICE tool, showing an editing efficiency of 38%. The F_0 founders carrying the *Adnp* variant were bred to WT C57BL/6 mice. HET mice were viable and fertile in both sexes and displayed no overt external abnormalities. However, the *Adnp* frameshift variant was transmitted at a lower-than-expected Mendelian ratio (26.1% of the offspring vs. expected 50%; 95% CI: 15.2–40.3%). At 10 weeks of age, HET mice weighed less than their WT littermates (WT: median 24.75 g, IQR 23.64–26.55; HET: median 22.34 g, IQR 20.00–23.88), corresponding to a mean difference of −2.41 g (95% CI: −4.20 to −0.48; Wilcoxon rank-sum test, p = 0.013) (Fig. 1C), and a subset developed recurrent eye infections and dental malocclusions (data not shown).

To verify expression of the mutant transcript, RT-PCR was performed on brain lysates using primers spanning the 14-bp deletion (Additional File S4). Targeted RT-PCR confirmed expression of the mutant transcript in HET mice (WT: 0.01 ± 0.09; HET: 1.07 ± 0.43), with levels exceeding background in WT mice (95% CI: 0.20 to 1.92; Student's t-test, p < 0.0001). Wild-type *Adnp* transcript levels were reduced in HET mice (WT: 1.01 ± 0.11; HET: 0.70 ± 0.06) by approximately 31% (95% CI: −0.58 to −0.035; Student's t-test, p = 0.023). RNA-sequencing (described below) of frontal cortex samples confirmed the presence of the 14-bp deletion with an allele frequency of 34.5% exclusively in the HET mice, consistent with RT-PCR findings (Additional File S5). Expression upstream of the mutation site was similar between genotypes (WT: 1.01 ± 0.17; HET: 0.97 ± 0.10) as shown in the global expression assay (95% CI: −0.24 to 0.31; Student's t-test, p = 0.98), in line with reports that suggest a regulatory feedback loop[72] (Fig. 1F). To assess whether the mutant mRNA yields a stable truncated Adnp protein, Western blotting of total brain extracts was performed, using validated C-terminal and N-terminal antibodies.[52] Using a C-terminal antibody, full-length Adnp protein levels were reduced in HET brains (WT: 0.86 ± 0.038; HET: 0.57 ± 0.10) by approximately 30% (95% CI: −0.46 to −0.14; Student's t-test, p = 0.0008). Consistent with our previous work,[52] no truncated protein was detected with the N-terminal antibody, and wild-type protein levels were not statistically different (WT: 1.00 ± 0.12; HET: 1.02 ± 0.06) between genotypes (95% CI: −0.14 to 0.46; Student's t-test, p = 0.96) (Fig. 1G). Together, these findings confirm that the 14-bp *Adnp* deletion reduces wild-type protein expression in HET mice and produces detectable mutant mRNA but no traceable truncated protein.

We next performed subcellular protein fractionation on whole brains to quantify Adnp across cytoplasmic, membrane-bound, nuclear-soluble, chromatin-bound, and cytoskeletal fractions. Adnp abundance was lower in chromatin-bound fractions of HET mice as detected by N-terminal (mean difference = −0.26 ± 0.05; 95% CI: −0.42 to −0.10; Student's t-test, p = 0.003) and C-terminal (mean difference = −0.74 ± 0.11; 95% CI: −1.10 to −0.38; Student's t-test, p = 0.001) antibodies. The C-terminal detection further showed no statistically significant difference in Adnp levels in the nuclear-soluble fraction (mean difference = −0.35 ± 0.09; 95% CI: −0.60 to −0.10; Student's t-test, p = 0.082), while cytoskeletal Adnp levels were reduced (mean difference = −0.51 ± 0.10; 95% CI: −0.75 to −0.26; Student's t-test, p = 0.002) (Fig. 2A–D). ADNP bands were detected at multiple molecular weights, but no genotype-dependent differences were observed in cytoplasmic or membrane-bound fractions, possibly reflecting proteolytic processing or degradation.[52] Overall, these data indicate that the *Adnp* frameshift variant reduces protein levels in chromatin-bound and nuclear-soluble compartments, implying disrupted coordination between nuclear and cytoskeletal functions, consistent with a moonlighting role of Adnp across both compartments.

Given that Adnp interacts with several chromatin remodellers[4] and exerts a repressive function during development,[48,51] we examined chromatin accessibility using the assay for transposase-accessible chromatin sequencing (ATAC-seq) on frontal cortex tissue. Genome-wide ATAC-seq signals were increased in HET mice, indicating a global rise in chromatin accessibility (Fig. 2E). Because transcriptional up- and down-regulation are often associated with corresponding changes in accessibility,[73] we analysed ATAC-seq signals at transcription start sites (TSSs) of differentially expressed genes identified by bulk RNA-seq (described below). Chromatin accessibility was elevated at TSSs of all deregulated genes, regardless of the direction of the expression change (Fig. 2F–H), supporting a genome-wide increase in chromatin accessibility in HET mice. Collectively, these findings indicate a partial loss of Adnp's repressive function due to reduced protein abundance, resulting in increased genome-wide chromatin accessibility in the HET brain.

Adnp mice show distinct neuroanatomical changes

We next examined whether the *Adnp* frameshift variant alters brain morphology, as a substantial part of

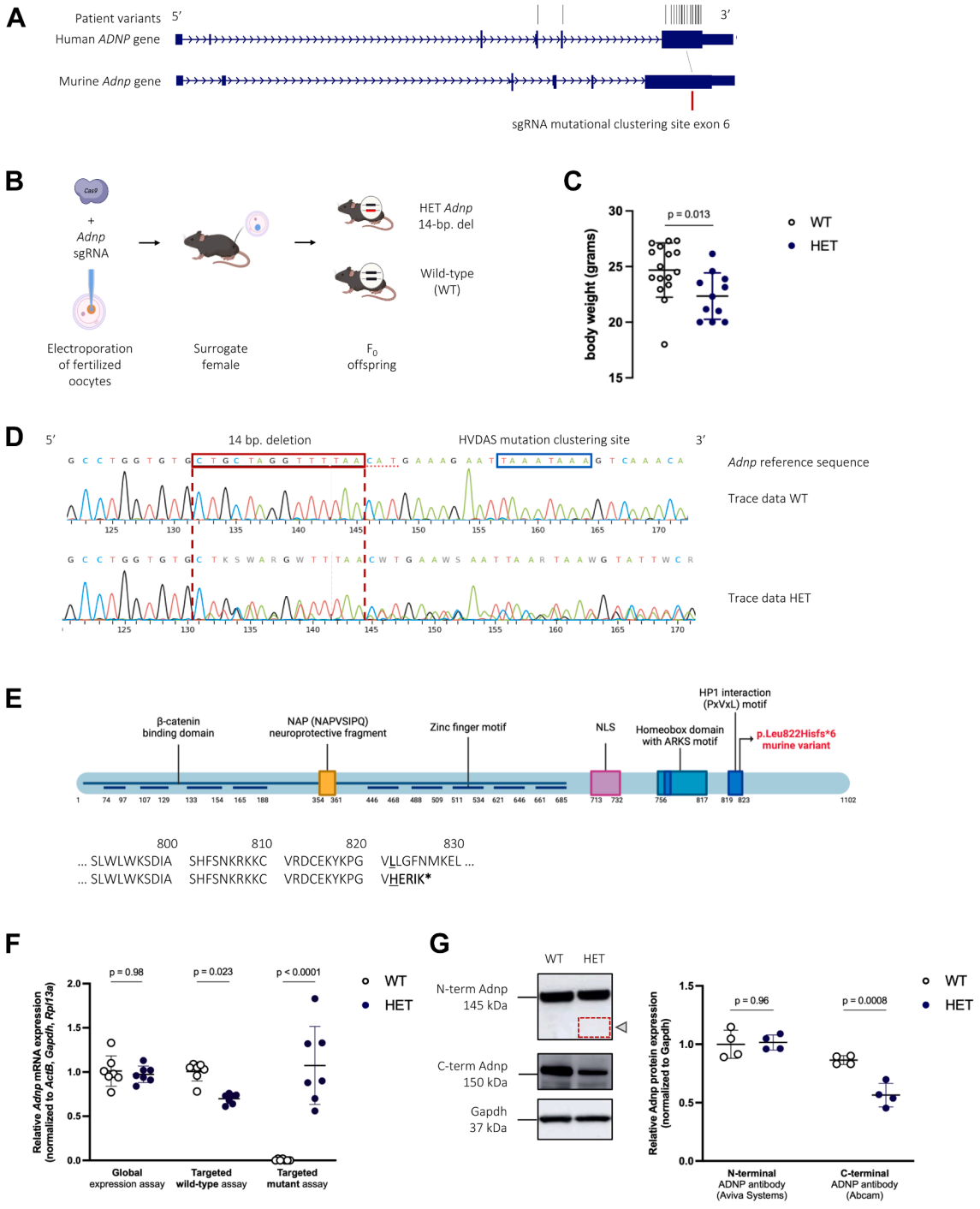

Fig. 1: **Generation and characterisation of the *Adnp* heterozygous (HET) mouse model. (A)** Location of patient variants across the human *ADNP* gene and designed sgRNA targeting a mutational hotspot in exon 6 of the murine *Adnp* gene. **(B)** Mouse line generation. HET = heterozygous; bp = base pair; del = deletion. **(C)** Body weight WT (n = 16) and HET (n = 11) mice. Median weight: WT = 24.75 g; HET = 22.34 g. Data are shown as median with IQR, p = 0.013 (Wilcoxon rank-sum test). **(D)** Sanger sequencing showing the heterozygous 14-bp deletion (red box, 5′-CTGCTAGGTTTTAA-3′) in exon 6 near a patient mutational hotspot (blue box, 5′-TAAATAAA-3′). **(E)** Schematic representation of the murine Adnp protein showing major functional domains: β-catenin-binding region, NAP neuroprotective fragment, zinc fingers, nuclear localisation signal (NLS), homoeobox domain, and heterochromatin protein 1 (HP1) interaction motif, harbouring the p.Leu822Hisfs*6 frameshift variant. Wild-type and mutant protein sequences, showing a premature stop codon. (**F**) RT-PCR analysis

patients presents with cerebral abnormalities, including atypical white matter lesions, delayed myelination, cortical dysplasia or atrophy, perinatal hypoxic-ischaemic encephalopathy, hydrocephalus, and hippocampal hypoplasia.[16]

To assess finer-scale neuroanatomical changes in HET mice, we applied a validated, blinded morphometric protocol, quantifying 40 parameters across 22 distinct brain regions on sagittal sections at +0.60 mm lateral.[35] Genotype-associated differences were observed in five neuroanatomical measures (Additional File S6). The motor cortex, which supports executive functions, was reduced in HET mice by approximately 15% in length (WT: 0.14 ± 0.0041 cm; HET: 0.12 ± 0.01 cm; 95% CI: –0.038 to –0.0031; Student's t-test, p = 0.0061). The internal granular layer of the cerebellum, associated with motor coordination, was 17% smaller (WT: 0.036 ± 0.0033 cm^2; HET: 0.030 ± 0.0045 cm^2; 95% CI: –0.012 to –0.0048; Student's t-test, p = 0.037), and the total thalamic area, serving as a subcortical relay, was reduced by 12% (WT: 0.031 ± 0.0022 cm^2; HET: 0.027 ± 0.0024 cm^2; 95% CI: –0.0071 to –0.00071; Student's t-test, p = 0.021). In contrast, the internal pyramidal layer of the hippocampus, a region involved in learning and memory, was larger in HET mice by approximately 35% (WT: 0.0012 ± 0.00015 cm^2; HET: 0.0017 ± 0.00019 cm^2; 95% CI: 0.00016 to 0.00070; Student's t-test, p = 0.008). The pontine nuclei, which regulate motor output and sleep, exhibited a marked 41% decrease in size (WT: 0.0035 ± 0.00058 cm^2; HET: 0.0021 ± 0.00075 cm^2; 95% CI: –0.0025 to –0.00041; Student's t-test, p = 0.016) (Fig. 3A). Myelin staining of paraffin-embedded sections confirmed the enlarged CA1 hippocampal region and revealed subtle histomorphological changes within the thalamus of HET mice (Fig. 3B). Collectively, this comprehensive neuroanatomical assessment indicates that the heterozygous *Adnp* frameshift variant induces mild but distinct alterations in regional brain morphology.

To localise Adnp within the affected regions, frozen brain sections were immunolabeled for ADNP in the motor cortex, the hippocampus, and the cerebellum, regions identified as morphologically altered in HET mice (Additional File S7). Adnp immunofluorescence revealed predominantly nuclear localisation, evidenced by colocalisation of DAPI (blue) and Cy3 (red) signals in all three regions (Fig. 3C). Nuclear Adnp intensity was lower in HET mice across the cortex (mean difference = –7.73 ± 1.39; 95% CI: –10.76 to –4.70; Student's t-test, p = 0.039), hippocampus (mean difference = –18.47 ± 4.67; 95% CI: –28.64 to –8.31; Student's t-test, p < 0.0001), and cerebellum (mean difference = –6.67 ± 2.06; 95% CI: –11.16 to –2.17; Student's t-test, p = 0.041) compared to WT littermates (Fig. 3D).

Behavioural phenotyping of adolescent Adnp HET mice reveals cognitive impairments, repetitive behaviour, increased anxiety, and altered sociability

To assess the functional consequences of the *Adnp* frameshift variant, we conducted a comprehensive behavioural battery in two independent cohorts of male adolescent WT and HET littermate mice, encompassing cognitive, motor, repetitive, and social domains.

Hippocampus-dependent visual-spatial learning was assessed using the Morris water maze (MWM) test. HET mice travelled longer paths during acquisition (mean difference: 291.3 ± 102 cm; 95% CI: 86.80–495.8 cm; 2-way repeated measures ANOVA, p = 0.0065) and were slower in escape latency (mean difference: 51.89 ± 11.66 s; 95% CI: 28.52–75.26 s; 2-way repeated measures ANOVA, p = 0.042), indicating impaired spatial learning (Fig. 4A and B). Swim speed was also reduced (mean difference: –3.78 ± 0.79 cm/s; 95% CI: –5.39 to –2.19 cm/s; 2-way repeated measures ANOVA, p = 0.016) in HET mice compared to WT littermates (Fig. 4C). During the probe trial, the percentage of time spent in the target quadrant was not statistically different between genotypes (mean difference: –0.00088 ± 0.0011 s; 95% CI: –0.0013 to 0.0031 s; 2-way repeated measures ANOVA, p = 0.69), nor the number of target entries (mean difference: 0.043 ± 0.88; 95% CI: –1.74 to 1.84; 2-way repeated measures ANOVA, p = 0.60).

Fear- and context-associated learning were evaluated using the passive avoidance test. Latency to enter the dark compartment did not differ during training (mean difference: 3.94 ± 2.27 s; 95% CI: –0.70 to 8.58 s; Student's t-test, p = 0.79) or test phase (mean difference: 10.63 ± 6.67 s; 95% CI: –3.39 to 24.65 s; Student's t-test, p = 0.20), indicating no profound fear- or context-related deficits in learning and memory (Fig. 4D).

Motor coordination was assessed on the accelerating rotarod. Contrary to clinical features such as hypotonia and gait disturbances reported in patients,[16] HET mice showed a comparable time on the rod to their WT littermates across trial blocks (mean difference: –17.10 ± 6.11 s; 95% CI: –110 to 75; 2-way repeated measures ANOVA, p = 0.88), suggesting preserved motor coordination under the tested conditions (Fig. 4E).

demonstrating reduced *Adnp* mRNA in HET brains (targeted wild-type assay), p = 0.023 (Student's t-test) and mutant transcript expression (targeted mutant assay), p < 0.0001 (Student's t-test). Expression upstream of the deletion (global assay) was unchanged between genotypes, p = 0.98 (Student's t-test). WT: n = 7, HET: n = 7. Data are shown as mean ± s.d. **(G)** Western blot analysis showing reduced full-length Adnp with the C-terminal antibody, p = 0.0008 (Student's t-test), but not the N-terminal antibody, p = 0.96 (Student's t-test). Gapdh was used for normalisation. WT: n = 4, HET: n = 4. Data are shown as mean ± s.d.

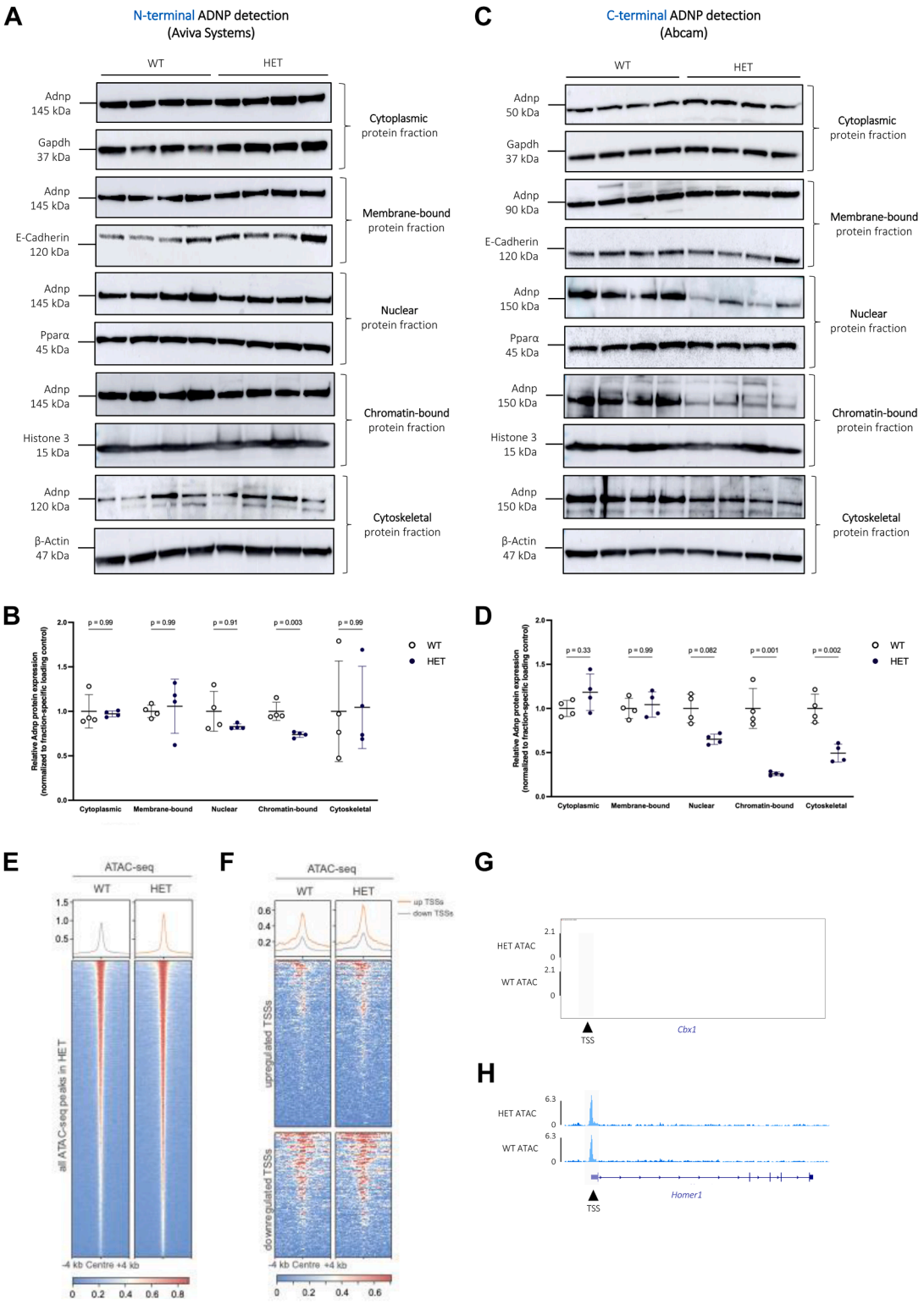

Fig. 2: **Western blot and ATAC-seq analyses of Adnp in fractionated brain compartments reveal altered chromatin association and accessibility.** Proteins were sequentially extracted using cytoplasmic (CEB), membrane (MEB), nuclear-soluble (NEB), chromatin-bound (CHR), and cytoskeletal (PEB) extraction buffers. Immunoblots were probed with N- or C-terminal Adnp antibodies and normalised to fraction-

Anxiety-like behaviour was evaluated in the elevated plus maze. HET mice spent less time in the open arms (mean difference: –33.61 ± 10.58 s; 95% CI: –55.26 to –11.97 s; Student's t-test, p = 0.0035), whereas total distance travelled (mean difference: –270 ± 154.8 cm; 95% CI: –589.6 to 43.49 cm; Student's t-test, p = 0.088) and time spent in the closed arms (mean difference: –35.45 ± 23.21 s; 95% CI: –82.93 to 12.02 s; Student's t-test, p = 0.12) were not statistically different between genotypes (Fig. 4F–I). The time spent in the open arms was approximately half that of WT controls, consistent with increased anxiety-like behaviour. No statistical differences were detected in the number of entries into open (mean difference: –4.04 ± 2.54; 95% CI: –9.25 to 1.16; Student's t-test, p = 0.12) or closed (mean difference: –3.14 ± 3.17; 95% CI: –3.40 to 9.70; Student's t-test, p = 0.22) arms (Fig. 4H–J).

Restricted and repetitive behaviours were measured in the marble-burying test as a readout for ASD, a clinical hallmark of patients with Helsmoortel-Van der Aa syndrome.[16] HET mice buried more marbles than WT controls (WT: median 2, IQR 2–6; HET: median 7, IQR 3–9), corresponding to a mean difference of 5.0 (95% CI: 0.01–5.27; Wilcoxon rank-sum test, p = 0.045) (Fig. 4K), indicating increased repetitive behaviour.

Social interest was assessed in two complementary paradigms. In the social exploration assay, male HET mice travelled shorter distances when interacting with either a female (mean difference: –506.6 ± 211.2 cm; 95% CI: –939.3 to –73.92 cm; Student's t-test, p = 0.023) or male (mean difference: –444.9 ± 213.1 cm; 95% CI: –882.1 to –7.65 cm; Student's t-test, p = 0.046) stranger mouse (Fig. 4L–P). For the female stranger mouse, male HET mice also showed reduced distance (mean difference: –1018 ± 276.2 cm; 95% CI: –1583 to –451.9 cm; Student's t-test, p = 0.001), shorter duration (mean difference: –130.5 ± 37.97 s; 95% CI: –208.3 to –52.74 s; Student's t-test, p = 0.0019), and fewer entries into the centre zone (mean difference: –25.3 ± 9.7%; 95% CI: –45.7 to –4.9%; Student's t-test, p = 0.048), suggesting decreased exploratory and social behaviour (Fig. 4N–O). We detected no genotype-dependent differences in travelled distance (mean difference: –183.1 ± 282.9 cm; 95% CI: –763.5 to 397.3 cm; Student's t-test, p = 0.52), duration (mean difference: –40.61 ± 41.05 s; 95% CI: –124.8 to 43.63 s; Student's t-test, p = 0.33), or entries into the centre circle (mean difference: –11.7 ± 10.4%; 95% CI: –33.6 to 10.2%; Student's t-test, p = 0.60) during exploration of a male stranger (Fig. 4Q–S). The three-chamber test confirmed these findings. Both genotypes preferred the chamber containing a stranger mouse over a covered object (mean WT difference: 51.93 ± 8.84 s; 95% CI: 33.89–69.98 s and mean HET difference: 47.38 ± 9.82 s; 95% CI: 27.26–67.49 s; 2-way ANOVA, p < 0.0001), demonstrating intact sociability overall. However, HET mice spent less time interacting with the stranger mouse (mean difference: –25.87 ± 9.57 s; 95% CI: –45.6 to –6.1 s; 2-way ANOVA, p = 0.035) and were slower (mean difference: –809.7 ± 151.2 cm; 95% CI: –1119 to –500.5 cm; 2-way ANOVA, p < 0.0001) than WT littermates (Fig. 4T). In the social novelty phase, both groups showed comparable preferences for the novel versus familiar stranger mouse (mean WT difference: 16.99 ± 17.57 s; 95% CI: –20.46 to 54.44 s; 2-way ANOVA, p = 0.40 and mean HET difference: 16.81 ± 15.12 s; 95% CI: –15.62 to 49.24 s; 2-way ANOVA, p = 0.95) (Fig. 4U).

Together, these results indicate that the *Adnp* frameshift variant elicits a constellation of behavioural abnormalities, including cognitive impairment, enhanced repetitive behaviour, anxiety-like traits, and reduced sociability, that recapitulates hallmark clinical features of Helsmoortel-Van der Aa syndrome patients.

To assess spontaneous behaviour in a naturalistic setting and in real time, we conducted 24-h live monitoring of freely moving WT and HET littermates using the Live Mouse Tracker (LMT) system.[40] Three cages containing four mice and five cages containing three mice of mixed genotypes were recorded. From these recordings, 33 behavioural traits were extracted for each individual mouse. Behavioural data were analysed using linear mixed-effects models (LMM) with genotype as a fixed effect and cage as a random effect, following normalisation of HET values to the mean of WT littermates within each cage. Genotype-associated differences were detected in a subset of LMT-derived behaviours (Additional File S8). In the domain of body configuration, HET mice spent less time sniffing the ground (head down) (mean difference = –0.30 ± 0.15; 95% CI: –0.43 to –0.17; LMM, p < 0.0001) and adopted a stretched-attend posture (SAP) more frequently (mean difference = 0.23 ± 0.06; 95% CI: 0.18–0.28; LMM, p = 0.0031), resulting in slower locomotion. They also displayed fewer rearing movements (rear isolated) (mean difference = –0.22 ± 0.20; 95% CI: –0.39 to –0.05; LMM, p = 0.0081), reflecting reduced

specific controls (Gapdh, E-cadherin, PPARα, histone H3, or β-actin). WT: n = 4, HET: n = 4. Data are shown as mean ± s.d. (**A and B**) N-terminal detection showing a significant Adnp reduction in the chromatin-bound fraction only, p = 0.003 (Student's t-test). (**C and D**) C-terminal detection showing reduced Adnp levels in nuclear-soluble, p = 0.082 (Student's t-test), chromatin-bound, p = 0.001 (Student's t-test), and cytoskeletal fractions, p = 0.002 (Student's t-test). (**E–H**) ATAC-seq heatmaps and genomic snapshot showing increased genome-wide chromatin accessibility in HET mice and specific loci (*Cbx1* and *Homer1*). WT: n = 2, HET: n = 2.

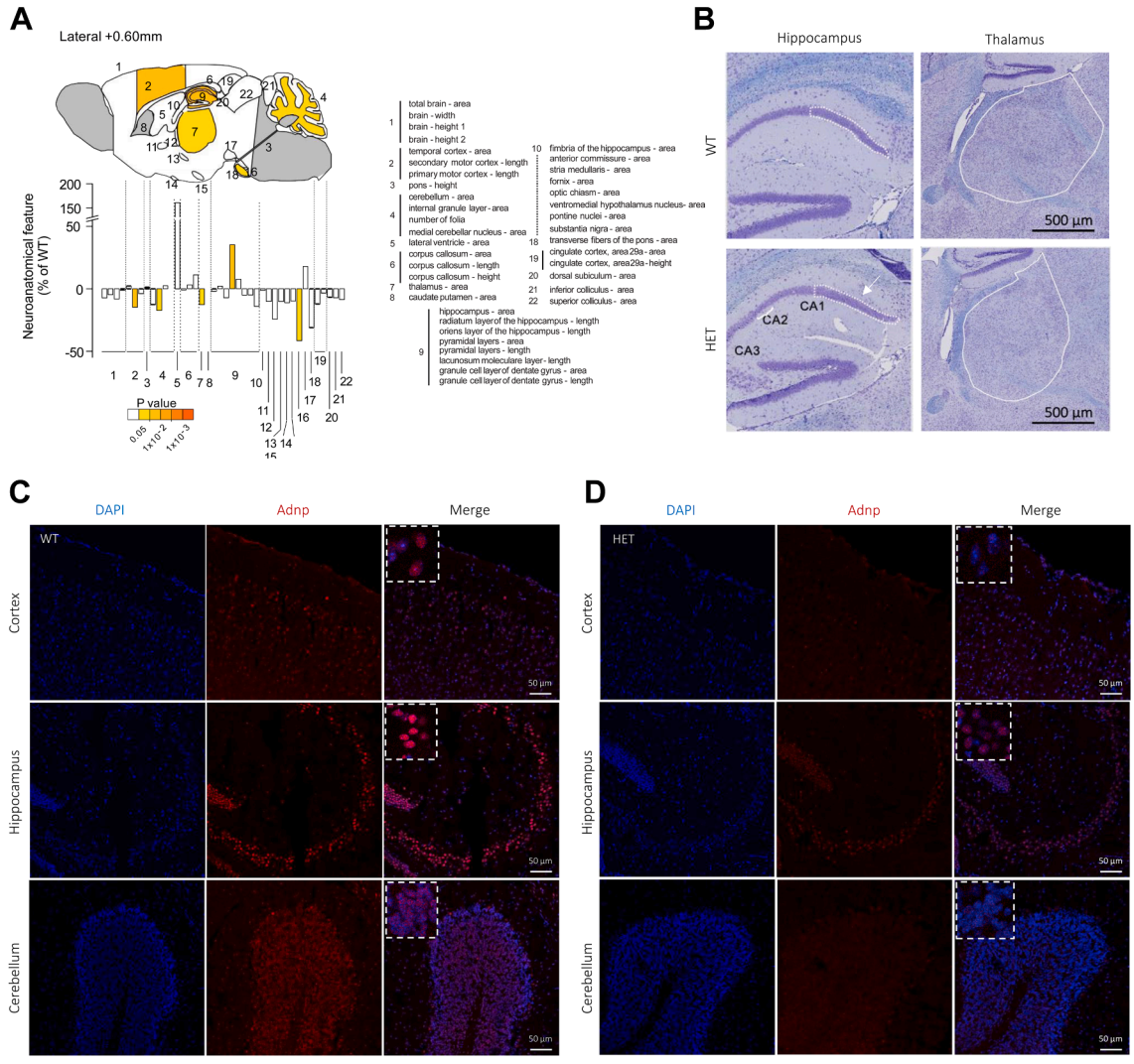

Fig. 3: **Subtle neuroanatomical changes and reduced Adnp levels in murine brain sections.** (**A**) Neuroanatomical mapping of WT and HET mice. Affected brain regions are plotted in sagittal planes. Colour shading corresponds to the magnitude of genotype-associated differences. P-values: white, $p > 0.05$; yellow, $p < 0.05$; grey, missing due to experimental artefacts. Numbers indicate assessed brain regions (1–22). Histograms show percentage change in HET compared to WT mice (WT = 100%). WT: n = 5, HET: n = 5. Data are shown as mean ± s.e.m., error bars were omitted for clarity in the schematic overview. (**B**) Stained sagittal brain sections from WT and HET littermates. CA1 pyramidal neurons of the hippocampus are enlarged by 35%, $p = 0.008$ (Student's t-test), whereas the total thalamic area is reduced by 12%, $p = 0.02$ (Student's t-test) in HET mice. (**C and D**) Adnp immunostaining in WT and HET mouse brain sections (motor cortex, hippocampus, and cerebellum). Adnp (red) localises predominantly to the nucleus (DAPI, blue) in all brain regions.

exploratory drive. During social interactions, HET mice moved more slowly and made less physical contact with cage mates, as shown by reduced move contact (mean difference = –0.054 ± 0.04; 95% CI: –0.09 to –0.018; LMM, p = 0.00016) and rear contact (mean difference = –0.17 ± 0.085; 95% CI: –0.25 to –0.093; LMM, p = 0.0002). Analysis of contact type revealed a decrease in nose-anogenital sniffing (mean difference = –0.063 ± 0.065; 95% CI: –0.12 to –0.004; LMM, p = 0.0074), potentially reflecting altered sexual interest, consistent with the observed lower breeding success in these animals. In addition, HET mice exhibited reduced social approach (mean difference = –0.096 ± 0.067; 95% CI: –0.16 to –0.035; LMM, p = 0.00071) and escape (mean difference = –0.024 ± 0.016; 95% CI: –0.038 to –0.01; LMM, p = 0.025) behaviours relative to WT littermates. Taken together, continuous tracking confirmed that HET mice exhibit a behaviour profile characterised by reduced locomotor activity, diminished social interest

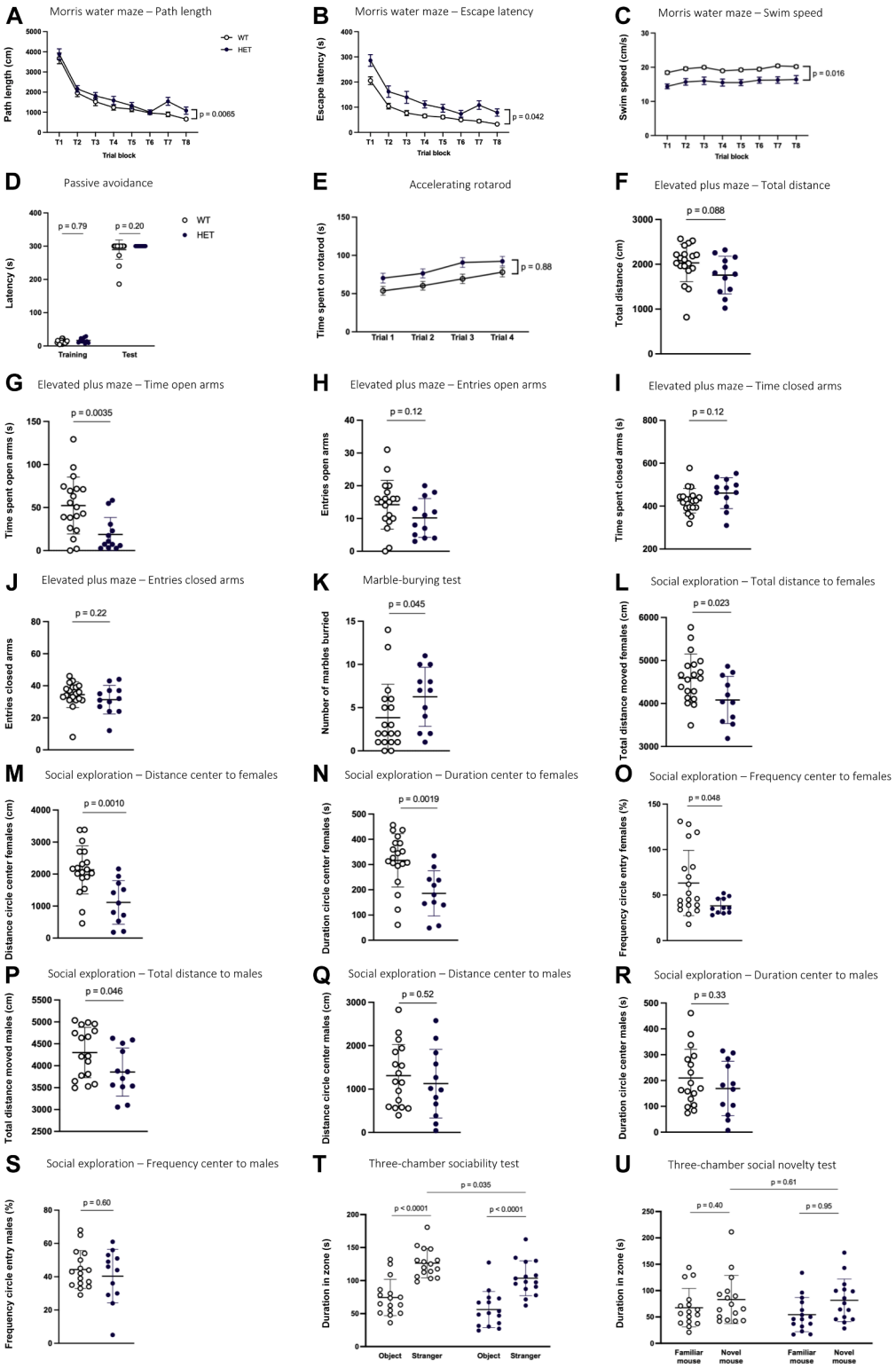

Fig. 4: **HET mice display cognitive impairment, repetitive behaviour, anxiety-like traits, and altered sociability.** (**A-C**) Morris water maze test. WT: n = 34, HET: n = 22. HET mice show increased path length, p = 0.0065 (two-way repeated measures ANOVA) and escape latency, p = 0.042 (two-way repeated measures ANOVA) compared with WT controls, indicating spatial learning deficits. Swim speed was reduced in

and exploration, and decreased exploratory behaviour, corroborating and extending findings from the individual behavioural assays.

Differential gene expression in the frontal cortex of adolescent HET mice reveals disrupted Wnt signalling and cytoskeletal imbalance contributing to impaired synaptic plasticity and lineage specification

To investigate the molecular consequences of the *Adnp* frameshift variant, we performed bulk RNA-seq of the frontal cortex, a region crucial for cognition, learning, and executive control,[74] in adolescent WT and HET littermates. After quality control and filtering, RNA from seven WT and seven HET mice was analysed across 13,383 expressed genes. Using stringent thresholds (FDR $\leq$0.05; p-adj. <0.05; $\log_2$FC > 0.5), we identified 348 downregulated and 646 upregulated genes (Additional File S9). Most expression changes in HET mice were modest, with the majority of genes showing an absolute log2FC < 1.5 (Fig. 5A). Sequence read alignment confirmed the 14-bp deletion (5′-GTTAAAACCTAGCA-3′) uniquely in HET libraries, verifying mutant transcript expression (RT-PCR, as described above). No difference in wild-type *Adnp* transcripts was observed between genotypes (WT $\log_2$CPM: 2.99 ± 0.10; HET $\log_2$CPM: 3.11 ± 0.33; 95% CI: –0.12 to 0.33; LMM, p = 0.31) (Fig. 5B), consistent with a compensatory feedback loop described previously.[72] Fast gene set enrichment analysis (fGSEA) revealed downregulation of Wnt signalling and actin cytoskeleton regulation by Rho GTPases, as well as upregulation of extracellular matrix-related processes (Fig. 5C). Functional enrichment of biological processes showed that upregulated genes were associated with synaptonemal complex organisation, keratinisation, neuron differentiation, and embryonic development. Downregulated genes were enriched for mitochondrial respiratory chain components, glutamate receptor signalling, dendritic spine development, and synaptic plasticity (Additional File S10).

We validated and confirmed the differential expression of sixteen representative genes by RT-PCR. We showed downregulation of *Wnt10a* (mean difference: –0.90 ± 0.29; 95% CI: –1.53 to –0.27; Student's t-test, p = 0.0091) and *Dkk3* (mean difference: –0.78 ± 0.24; 95% CI: –1.31 to –0.25; Student's t-test, p = 0.0073), implicating impaired Wnt signalling in HET mice. Also in line with the RNA-seq results, the endodermal differentiation factor *Igfbp4* (mean difference: 2.63 ± 0.34; 95% CI: 1.89–3.38; Student's t-test, p = 0.011) and the lineage-determining transcription factors *Otx2* (mean difference: 2.05 ± 0.93; 95% CI: 0.01 to 4.10; Student's t-test, p = 0.0022), *Gata2* (mean difference: 0.78 ± 0.30; 95% CI: 0.13 to 1.43; Student's t-test, p = 0.047), and *Pax5* (mean difference: 1.70 ± 0.46; 95% CI: 0.70 to 2.69; Student's t-test, p = 0.018) were upregulated, whereas the transcription factor *Pou4f1* (mean difference: –0.64 ± 0.16; 95% CI: –0.98 to –0.30; Student's t-test, p = 0.033) was downregulated in HET mice compared to WT littermates. Genes regulating postsynaptic structure and function were also affected, including *Homer1* (mean difference: –0.48 ± 0.17; 95% CI: –0.86 to –0.10; Student's t-test, p = 0.017) and *Arc* (mean difference: –0.81 ± 0.22; 95% CI: –1.30 to –0.32; Student's t-test, p = 0.0034) were downregulated, while *Camk2d* (mean difference: 0.50 ± 0.18; 95% CI: 0.12–0.88; Student's t-test, p = 0.014) and *Grin2d* (mean difference: 0.94 ± 0.41; 95% CI: 0.05–1.83; Student's t-test, p = 0.041) were upregulated, alongside reduced *Bdnf* expression (mean difference: –0.55 ± 0.18; 95% CI: –0.94 to –0.16; Student's t-test, p = 0.0092). Presynaptic and neurotransmitter genes showed a similar imbalance, with reduced *Stx1a* (mean difference: –0.54 ± 0.17; 95% CI: –0.92 to –0.16; Student's t-test, p = 0.0088) and *Kcnh7* (mean difference: –0.53 ± 0.19; 95% CI: –0.95 to –0.11; Student's t-test, p = 0.018) expression, but elevated *Syt10* (mean difference: 0.49 ± 0.19; 95% CI: 0.066–0.91; Student's t-test, p = 0.027) and *Gabbr2* (mean difference: 1.83 ± 0.61; 95% CI: 0.50–3.17; Student's t-test,

HET mice compared with WT controls, p = 0.016 (two-way repeated measures ANOVA). (**D**) Passive avoidance. WT: n = 19, HET: n = 11. No significant genotype differences in latency to the dark compartment during training, p = 0.79 (Student's t-test) or testing, p = 0.20 (Student's t-test). (**E**) Accelerating rotarod. WT: n = 35, HET: n = 27. HET mice remained on the rod for a comparable duration to WT littermates, p = 0.98 (two-way repeated measures ANOVA). (**F-J**) Elevated plus maze. WT: n = 19, HET: n = 12. HET mice spent less time in the open arms, indicating increased anxiety, p = 0.0035 (Student's t-test). Total distance travelled, p = 0.088 (Student's t-test), duration, p = 0.12 (Student's t-test), and the number of closed arm entries, p = 0.22 (Student's t-test) were comparable between genotypes. (**K**) Marble burying. WT: n = 19, HET: n = 11. HET mice buried more marbles than WT mice, indicating increased repetitive behaviour, p = 0.045 (Wilcoxon rank-sum test). (**L–O**) Social exploration with female strangers. WT: n = 19, HET: n = 11. Male HET mice show reduced distance travelled, p = 0.023 (Student's t-test), duration, p = 0.0019 (Student's t-test), and entries in the centre zone, p = 0.048 (Student's t-test). (**P–S**) Social exploration with male strangers. WT: n = 19, HET: n = 11. Male HET mice exhibit no significant differences in distance, p = 0.046 (Student's t-test), duration p = 0.33 (Student's t-test), and entries in the centre zone, p = 0.60 (Student's t-test). (**T**) Three-chamber sociability test. WT: n = 16, HET: n = 15. Both genotypes prefer a stranger mouse over an object, p < 0.0001 (two-way ANOVA), but HET mice are less active, slower, and spend less time with the stranger mouse, p = 0.035 (two-way ANOVA). (**U**) Three-chamber social novelty test. WT: n = 16, HET: n = 15. Both genotypes show comparable interest in the novel stranger mouse, p > 0.40 (two-way ANOVA). Data are presented as mean ± s.d. for parametric tests, respectively as median ± IQR for non-parametric tests.

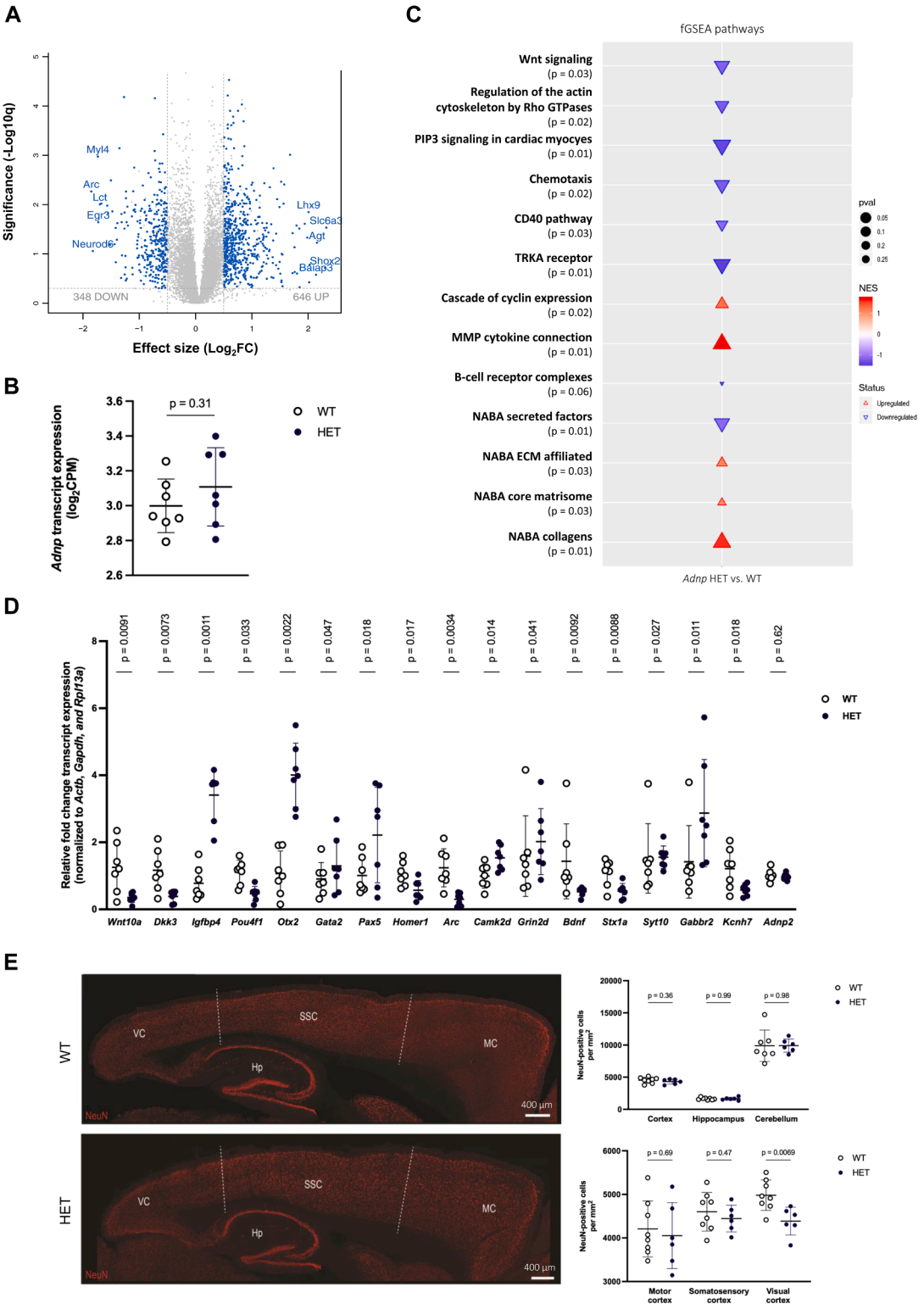

Fig. 5: **Transcriptomic and histological alterations in the frontal cortex of HET mice.** (**A**) Volcano plot of DEGs showing modest effect sizes (log_2FC). (**B**) *Adnp* transcript levels were similar between genotypes, with no evidence for differential expression detected, p = 0.31 (LMM), consistent with the possibility of autoregulatory mechanisms. WT: n = 7, HET: n = 7. Error bars show the mean log (counts per million,

p = 0.011) transcripts. *Adnp2*, a paralogue of *Adnp* that was not differentially expressed in the RNA-seq data, served as a negative control and showed a similar expression between genotypes (mean difference: –0.037 ± 0.07; 95% CI: –0.20 to 0.12; Student's t-test, p = 0.62) (Fig. 5D).

Given *Adnp's* role as a chromatin-associated transcription regulator, we examined transcription factor (TF) motif enrichment among DEGs. We identified a co-expressed module of 263 genes, enriched for TFs linked to upregulated genes, consistent with global transcriptional activation following *Adnp* loss. Upregulated TFs included POU-class (*Pou3f1/6f2/2f1*), homoeobox (*Hoxb5/c8/a11/d11*), pluripotency factors (*Nanog, Sox2, and Pax4/6/7*), and chromatin remodellers (*Yy1* and *Kdm2a/b*), mirroring reported features of *Adnp* haploinsufficiency.[25] Downregulated TFs included *Atf4 and Atf5*, implicated in Coffin-Lowry syndrome.[75] Shared TFs, notably *Gata2/4/6*, regulate chromatin binding and stem cell differentiation[76] (Additional File S11).

Because both Wnt and actin cytoskeletal pathways are essential for neuronal differentiation,[76] we next assessed whether *Adnp* deficiency affected neural cell populations. Immunostaining for the neuronal marker NeuN was comparable in the hippocampus (mean difference: –0.50 ± 309.7; 95% CI: –1515 to 1514; Student's t-test, p = 0.99), cerebellum (mean difference: –27.41 ± 604; 95% CI: –1588 to 1533; Student's t-test, p = 0.98), and cortex (mean difference: –239.8 ± 569; 95% CI: –722.40 to 242.80; Student's t-test, p = 0.36), although the numeric values of cortical NeuN-positive cell counts trended lower in HET mice. Subregional analysis identified a significant reduction in the visual cortex (mean difference: –595.2 ± 475.5; 95% CI: –997 to –193; Student's t-test, p = 0.0069), whereas no statistical differences were detected in the motor (mean difference: –218.6 ± 980; 95% CI: –1073 to 636; Student's t-test, p = 0.69) and somatosensory cortex (mean difference: –119.2 ± 479; 95% CI: –523 to 285; Student's t-test, p = 0.47) (Fig. 5E). The microglial marker Iba1 showed no significant differences in the hippocampus (mean difference: –21.90 ± 43.50; 95% CI: –59.12 to 15.34; Student's t-test, p = 0.25) and cerebellum (mean difference: –28.31 ± 66.78; 95% CI: –33.51 to 90.12; Student's t-test, p = 0.29), but a mild, significant increase in Iba1-positive cells in the somatosensory cortex (mean difference: 68.5 ± 51.3; 95% CI: 21.22–115.82; Student's t-test, p = 0.029), suggesting localised microglial activation. Astrocytic marker Gfap staining showed no genotype-dependent differences across brain regions (mean difference: 0.065 ± 0.23; 95% CI: –0.39 to 0.52; 2-way ANOVA, p = 0.77) or cortical subregions (mean difference: 0.39 ± 0.19; 95% CI: –0.075 to 0.85; 2-way ANOVA, p = 0.54) (Additional File S12).

Taken together, transcriptomic and histological analyses demonstrate that *Adnp* deficiency leads to disrupted Wnt and cytoskeletal signalling, resulting in altered synaptic plasticity, misregulating lineage-specifying TFs, and cortical region-specific neuronal and microglial changes.

Adnp interacts with cytoskeletal regulators of synaptic plasticity and modulates glutamatergic signalling

Adnp heterozygosity was previously reported to impair synaptic plasticity in mice and humans.[12,28] Consistent with these findings, transcriptomic profiling in the cortex of HET mice revealed altered expression of genes linked to synaptic function. We therefore sought to identify direct Adnp-interacting partners involved in these pathways (Additional File S13). Differentially expressed gene clustering within synaptic plasticity pathways was analysed using STRING, revealing two major co-expression networks. The first network connected Adnp to Drebrin 1 (Dbn1) through the microtubule end-binding protein 3 (EB3), while a second involved Camk2a, a master regulator of synaptic plasticity,[77] together with Arc, Bdnf, and Grin2a, previously found dysregulated in the HET frontal cortex. *In situ* hybridisation of P28C57BL/6 brain sections showed punctate *Adnp* expression in the frontal cortex (white arrows), with overlapping enrichment of *Dbn1* and *Camk2a*, suggesting possible co-localisation. To confirm physical interactions, co-immunoprecipitation (CoIP) was performed from cortical lysates enriched for cytoskeletal and cytoplasmic proteins using ADNP-crosslinked agarose beads, followed by high-detergent washes to minimise nonspecific binding. The C-terminal ADNP antibody selectively precipitated the wild-type

CPM) ± s.d. (**C**) fGSEA of DEGs in the frontal cortex of HET versus WT mice. Each pathway is shown as a filled triangle positioned by its normalised enrichment score (NES). Triangle orientation denotes enrichment direction (upward = upregulated; downward = downregulated), with colour reflecting the NES (blue = negative, white = zero, red = positive). Triangle size indicates statistical significance, reported as p-values that are listed beneath each pathway. A size key (black circles) is provided for reference. (**D**) RT-PCR validation of sixteen DEGs, p < 0.05 (Student's t-test) and the *Adnp2* gene where no differential expression was detected, p = 0.62 (Student's t-test). WT: n = 7, HET: n = 7. Error bars represent mean logFC ± s.d. (**E**) Representative NeuN staining (red) in WT and HET mice (left) and quantification of NeuN-positive cells across cortex, p = 0.36 (Student's t-test), hippocampus (Hp), p = 0.99 (Student's t-test), and cerebellum (not shown), p = 0.98 (Student's t-test). Cortical subregions analysed: motor (MC), p = 0.69 (Student's t-test), somatosensory (SSC), p = 0.47 (Student's t-test), and visual (VS) cortex, p = 0.0069 (Student's t-test). Each condition included 3–4 randomly selected images. WT: n = 8, HET: n = 6. Data are shown as mean ± s.d.

protein, as the putative truncated isoform lacks the corresponding epitope.[52] Western blot analysis confirmed the specific elution of Adnp (150 kDa), Dbn1 (120 kDa), and Camk2a (50–60 kDa) in both genotypes. Across two independent biological replicates, quantification consistently revealed an increased Adnp-Dbn1 interaction (mean difference: 0.24 ± 0.06; 95% CI: 0.02–0.46) and reduced Adnp-Camk2a binding (mean difference: –0.42 ± 0.10; 95% CI: –0.64 to –0.20) in HET mice, suggesting dysregulated synaptic plasticity.

Eukaryotic Linear Motif (ELM) analysis identified several cytoskeleton- and calcium-associated motifs shared among Adnp (UniProt; Q9Z103), Dbn1 (UniProt; Q9QXS6), and Camk2a (UniProt; P11798) (Additional File S14). Multiple SH3 motifs in Adnp (aa189-195, FQHVAAP, p = 0.01), Dbn1 (aa284-290, AQRPDNP, p = 0.01), and Camk2a (aa205-211, ILLVGYP, p = 0.01) facilitate cytoskeletal interactions, complemented by S/TxIP-motifs in Adnp (aa354-361, NAPVSIPQ, p = 0.01) and Dbn1 (aa374-387, RRMAPTPIPTRSPS, p = 0.0002). Calcineurin-binding motifs were present in Adnp (aa894-899, PVFEVE, p = 0.001) and Dbn1 (aa683-688, PEIDIT, p = 0.0001), supporting a role in calcium signalling. Camk2a contained both a calmodulin-binding region (aa290-300, LKKFNARRKLK, p = 0.001) and an F-actin-binding site (aa284-287, QETV, p = 0.02), connecting cytoskeletal involvement to calcium-dependent synaptic plasticity.[78] Molecular docking using ClusPro and visualisation in ChimeraX predicted physical contact between the SxIP motif of Adnp (blue) and Dbn1 (grey), docking of Adnp within the Camk2a groove, consistent with the direct biochemical interaction.

Given the role of Adnp in regulating glutamatergic synapses[79] and calcium signalling,[80] we examined functional consequences in cortical synaptoneurosomes from WT and HET littermate mice (Additional File S13). Under unstimulated conditions, the ratio of Thr286-phosphorylated Camk2a to total Camk2a was significantly higher in HET mice compared to WT littermates (mean difference: 0.28 ± 0.19; 95% CI: 0.06–0.51; repeated measures ANOVA, p = 0.012). Following L-glutamate stimulation, the Thr286-Camk2a/Camk2a ratio significantly increased in WT synaptoneurosomes (mean difference: 0.18 ± 0.22; 95% CI: 0.007–0.35; repeated measures ANOVA, p = 0.042), whereas HET synaptoneurosomes exhibited a decrease relative to their unstimulated state (mean difference: –0.18 ± 0.22; 95% CI: –0.35 to 0.004; repeated measures ANOVA, p = 0.046). However, the interaction term of genotype and stimulation was small in magnitude (mean difference: –0.07 ± 0.29; 95% CI: –0.29 to 0.14; repeated measures ANOVA, p = 0.81), indicating that stimulation-induced changes were comparable between genotypes. Total Camk2a abundance was unchanged by genotype or stimulation (mean difference: 0.08 ± 0.20; 95% CI: –0.18 to 0.35; repeated measures ANOVA, p = 0.67), supporting an effect on phosphorylation rather than protein expression.

Collectively, these data demonstrate that Adnp interacts with Dbn1 and Camk2a through cytoskeletal and calcium-related motifs. Partial loss of wild-type Adnp alters these interactions, resulting in altered basal Camk2a phosphorylation and an atypical phosphorylation response in prepared synaptoneurosomes of HET mice.

Label-free proteomics reveals altered BAF complex and cytoskeletal protein expression

To identify post-transcriptional alteration not captured at the mRNA level,[81] we performed label-free quantitative proteomics (LFQ-MS) on frontal cortex lysates from adolescent WT and HET mice. Chromatographic reproducibility across different runs was high, yielding strong correlations between biological replicates (Additional File S15). Under a 1% FDR, approximately 2319 protein groups were identified per sample with fixed modifications of carbamidomethylation (C), deamidation (QN) and oxidation (M), including 9693 proteins with more than two unique peptides, 988 proteins with at least two, and 3646 with a single unique peptide. After quality-filtering of 3392 proteins, 98 showed significant differential expression (Additional File S16), of which 53 proteins were downregulated and 45 upregulated in HET brains (Student's t-test; p-adj <0.05) (Fig. 6A). Consistent with transcriptomic findings, several chromatin- and cytoskeletal proteins were dysregulated. Notably, two Adnp-interacting partners, heterochromatin Protein 1 homologue beta (HP1β) and BAF complex component Smarcc2, were upregulated among others, implicating aberrant chromatin remodelling.

Immunoblot validation confirmed increased HP1β (mean difference: 0.74 ± 0.20; 95% CI: 0.15–1.32; Student's t-test, p = 0.01) and Smarcc2 (mean difference: 0.51 ± 0.12; 95% CI: 0.21–0.81; Student's t-test, p = 0.007) expression in HET brains. In addition, we confirmed decreased Actn4 expression (mean difference: –0.36 ± 0.06; 95% CI: –0.53 to –0.19; Student's t-test, p = 0.004) in the HET brain, consistent with transcriptomic evidence of actin cytoskeletal disruption (Fig. 6B).

Pathway clustering of differentially expressed proteins (DEPs) using MetaScape revealed enrichment of actin filament bundle assembly, microtubule organisation, axon guidance, neurotransmitter regulation, neuronal development, and Rho GTPases signalling, closely overlapping with pathways identified by RNA-seq (Fig. 6C). Functional interacting mapping in STRING positioned ADNP within a network connecting HP1β and Smarcc2 (Fig. 6D), confirming its association with the BAF chromatin remodelling complex.[6]

Together, LFQ proteomics supports a model in which *Adnp* deficiency perturbs both nuclear chromatin

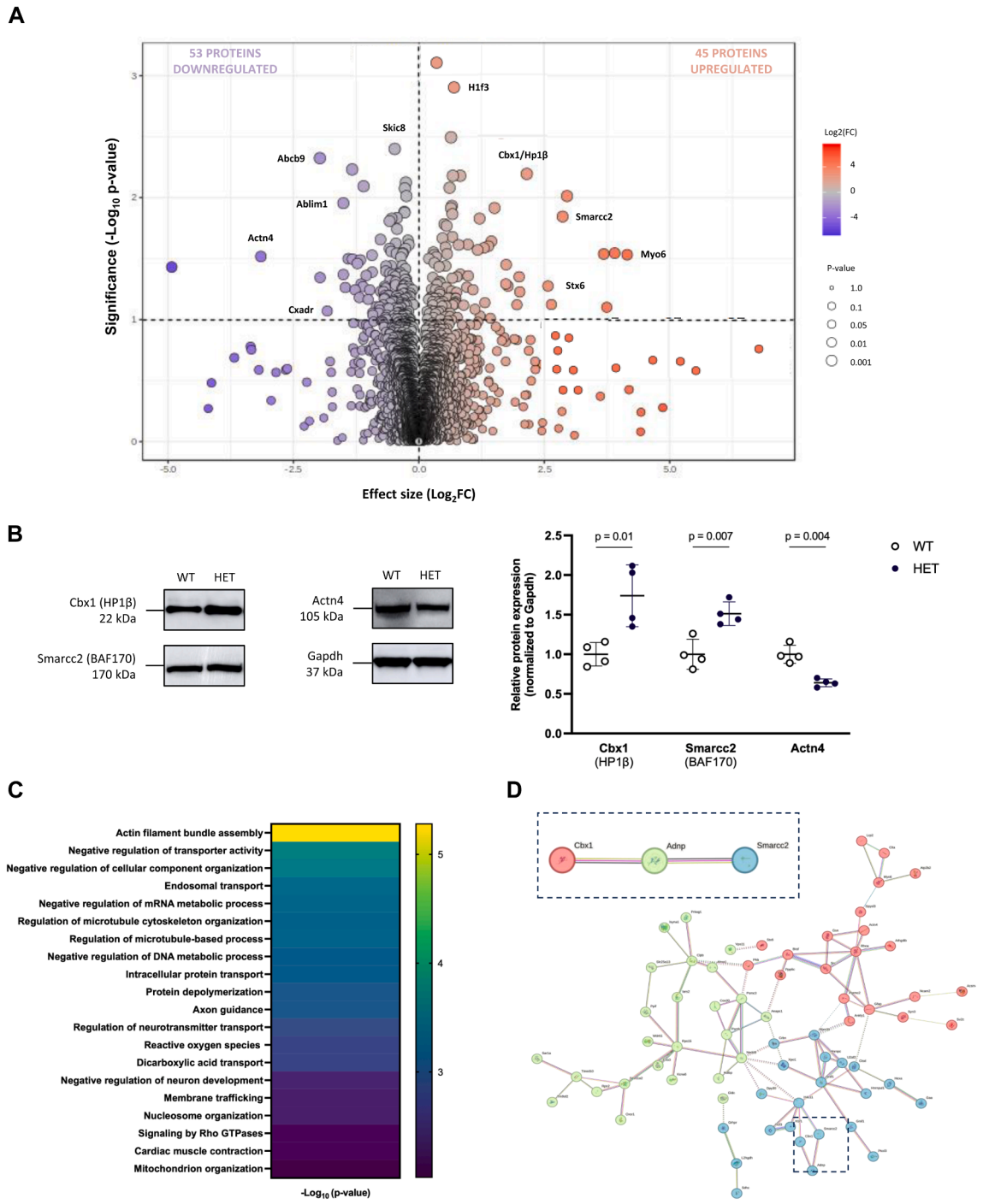

Fig. 6: **Discovery of altered SWI/SNF and cytoskeletal protein expression in HET brains.** (**A**) Volcano plot of DEPs in the frontal cortex, shown by the significance (-$\log_{10}$ p-value) and effect size ($\log_2$FC). Downregulated proteins in blue, upregulated in red. (**B**) Immunoblot validation of HP1β, p = 0.01 (Student's t-test), Smarcc2, p = 0.007 (Student's t-test), and Actn4, p = 0.004 (Student's t-test) expression, normalised to Gapdh. WT: n = 4, HET: n = 4. Data are shown as mean ± s.d. (**C**) Top 20 enriched Matascape pathways in the HET frontal cortex, represented by significance (-log p-value). (**D**) Predicted STRING protein–protein interaction network, integrating the DEPs. Adnp was found to interact with HP1β (Cbx1) and Smarcc2 (BAF170), consistent with BAF complex dysregulation. Proteins are represented by coloured network nodes in relation to each other. The edges represent functional associations supported by experimental or predicted evidence.

regulators and cytoskeletal components, converging on impaired neuron development and synaptic integrity.

The heterozygous Adnp variant induces local rearrangements in chromatin architecture

As Adnp, in complex with ChAHP, has been shown to modulate chromatin looping,[9] we investigated its *in vivo* contribution to 3D chromatin architecture in the frontal cortex of this disease-relevant HET mouse model. We performed *in situ* Hi-C on intact, crosslinked nuclei isolated from the frontal cortex of two independent WT and HET littermates. Following stringent quality control and validation of biological reproducibility, replicates were merged to obtain approximately 720 million and 620 million unique valid contacts from WT and HET mice, respectively (Additional File S17). Plotting cis-decay curves indicated no major alterations in contact frequencies across genomic distances following the heterozygous *Adnp* 14-bp deletion (Fig. 7A). The global interaction landscape revealed highly similar chromosome compartmentalisation between WT and HET mice, exemplified by chromosome 18 (Fig. 7B). Saddle plots displaying average contact enrichment between pairs of 100 kb loci, arranged by eigenvalue, confirmed this genome-wide similarity, showing no differences in A (active) or B (inactive) compartment interactions between genotypes (Fig. 7C). Visualisation of insulation profiles along chromosome 2, which harbours the *Adnp* gene, revealed no major differences between genotypes. Distribution analyses of insulation scores and topologically associating domains (TADs) sizes corroborated this observation genome-wide (Additional File S18). In addition, $\log_2$ insulation scores at TSSs of upregulated DEGs identified by RNA-seq showed no significant differences in genomic insulation between WT and HET mice (Additional File S18). Finally, normalised Hi-C contact profiles around chromatin loops indicated comparable loop strength between genotypes (WT: 3.71 ± 0.92; HET: 3.56 ± 0.52) (Fig. 7E). However, a focused analysis on genomic regions, previously identified as structurally altered in *Adnp* homozygous mESCs,[9] revealed three out of twelve loci with significant changes altered contact intensity in HET mice compared to WT littermates, corresponding to the *Abcc2, Cobll1*, and *Wnt5a* genes (Additional File S18). At the *Abcc2* locus, decreased looping in HET mice coincided with significant upregulation of *Abcc2* expression (RNA-seq; padj. = 0.007), consistent with the release of silencer-promoter constraints.[82] Conversely, increased looping at the *Cobll1* locus was associated with elevated *Cobll1* transcript levels (RNA-seq; padj. = 0.007). A similar correlation was observed for *Wnt5a*, where enhanced contact intensity parallelled increased *Wnt5a* mRNA expression (RNA-seq; padj. = 0.01) in HET mice compared to WT controls.

To complement the Hi-C data and directly address chromatin accessibility changes, we performed a focused ATAC-seq analysis on peaks within ±20 kb of TSSs of downregulated Wnt signalling genes and compared them to non-differentially expressed Wnt genes (Additional File S19). While global chromatin accessibility was elevated in HET mice, accessibility at downregulated Wnt loci remained unchanged, suggesting that these genes are subjected to locus-specific repressive mechanisms despite the overall chromatin decompaction.

Inspection of Hi-C contact matrices at additional deregulated Wnt signalling loci revealed disruption of a large (~500 kb) chromatin loop at the *Ccn4* locus in HET mice (Additional File S19). CTCF ChIP-seq data confirmed strong binding at the loop anchors, while *Satb1* binding was detected proximal to the distal anchor site. Given that *Satb1* is known to regulate genome topology and modulate Wnt target gene expression,[83–85] its reduced expression in HET mice (RNA-seq; padj. = 0.01), as detected by mRNA-seq, may contribute to altered 3D conformation and transcriptional repression of *Ccn4*, which further supports a mechanistic link between Adnp-associated chromatin architectural remodelling and Wnt pathway deregulation.

Taken together, these results demonstrate that the heterozygous *Adnp* 14 bp. deletion induces subtle, locus-specific rearrangements in chromatin architecture in the mouse frontal cortex that correlate with transcriptional alterations. These include disrupted silencer-promoter interactions (*Abcc2*), reinforced enhancer-promoter contacts (*Cobll1, Wnt5a*), and altered 3D conformation at the *Ccn4* locus, which may reflect context-dependent dysregulation of Wnt signalling architecture.

Discussion

The *Adnp* frameshift mouse model introduces a heterozygous 14-bp deletion within a mutational hotspot of the human gene associated with Helsmoortel-Van der Aa syndrome. The variant generates a premature stop codon and a truncated transcript. No truncated protein could be detected by Western blotting. However, a 30% decrease of wild-type protein was detected in total cortical protein lysates by Western blotting, while wild-type Adnp protein levels were reduced by approximately 50% in the motor cortex, hippocampus, and cerebellum, as shown by immunocytochemistry. Protein fractionation further confirmed the 50% loss from chromatin-enriched compartments, consistent with partial loss of Adnp's chromatin-repressive function. ATAC-seq analysis revealed increased chromatin accessibility, reinforcing the correlation between Adnp deficiency and epigenetic dysregulation. Moreover, frameshift mice had a lower bodyweight and displayed recurrent eye irritations, dental malocclusion, and a behavioural profile encompassing cognitive impairment, repetitive activity, anxiety-like behaviour, and

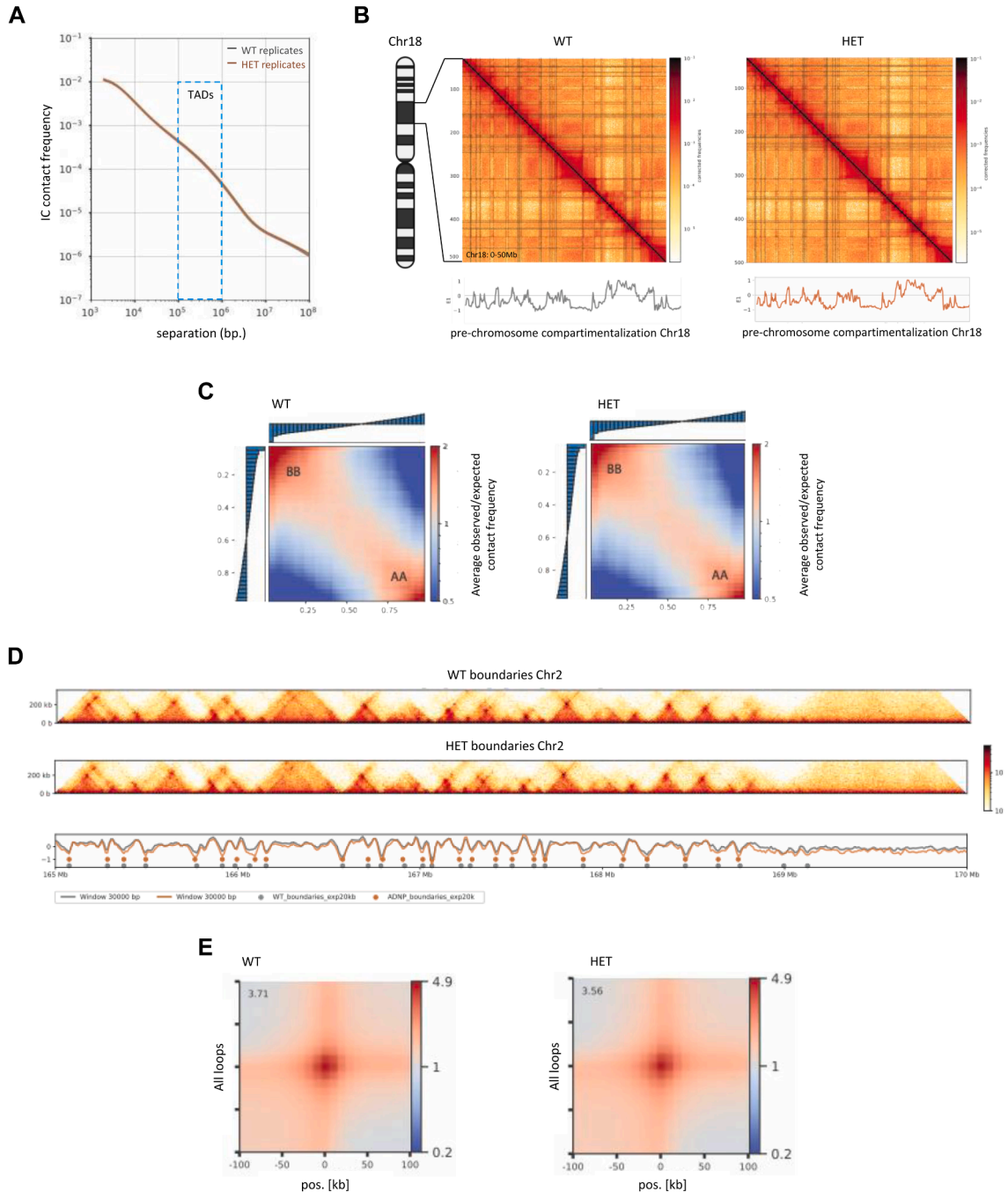

Fig. 7: **The heterozygous *Adnp* variant does not induce global changes in 3D genome architecture.** (**A**) Cis-decay contact probability curves of merged datasets showing normalised cis contact frequency relative to genomic distance. (**B**) Contact matrix showing the 0–50 Mb region of chromosome 18 in *Adnp* WT (left panel) and HET (right panel) frontal cortex at 100-kb resolution. The line plot shows binary segmentation of the first eigenvector, with positive values corresponding to A compartments and negative values corresponding to B compartments. (**C**) Saddle plots showing average observed/expected contact frequencies in inactive (B compartments, top left) and active (A compartments, bottom right) chromatin in *Adnp* WT and HET datasets. (**D**) Interaction matrix showing a segment of chromosome 2 at 10-kb resolution. The line plot shows insulation scores calculated using a 30-kb window size. Dots indicate the positions of TAD boundaries in WT and HET datasets. (**E**) Aggregate plots showing normalised Hi-C signal around all loops identified in the WT and HET datasets. WT: n = 2, HET: n = 2.

altered sociability, closely parallelling patient features. At the molecular level, RNA sequencing of the frontal cortex identified Wnt signalling and cytoskeletal pathway dysregulation, suggesting convergence toward impaired synaptic plasticity. This interpretation was strengthened by altered interactions between Adnp, Dbn1, and Camk2a, and by altered phosphorylation responses to L-glutamate in synaptoneurosomes. Mass spectrometry further confirmed dysregulation of Wnt signalling and cytoskeletal pathways, including BAF complex expression alterations and downregulation of actin-associated proteins. Despite multiple chromatin remodelling interactions, Hi-C analysis showed no genome-wide rearrangements in chromatin architecture.

To summarise, the *Adnp* frameshift mouse model, harbouring the heterozygous p.Leu822His*6 variant, recapitulates a prevalent patient-like variant, providing an integrated view of how partial Adnp loss perturbs chromatin regulation, Wnt signalling, and cytoskeletal pathway alterations. These convergent mechanisms elucidate key disease processes in Helsmoortel-Van der Aa syndrome and highlight translational avenues for therapeutic targeting.

The *Adnp* frameshift mouse exhibited reduced body weight and approximately 35–50% lower levels of wild-type transcript and protein. Recurrent eye infections[86] and dental malformations, previously reported in haploinsufficient (Δexons 1–6 or Δexon 6) mice,[87] as well as in a subset of patients were also observed.[16] Behavioural testing revealed decreased spatial learning in the MWM test, increased anxiety-like behaviour in the elevated plus maze, repetitive behaviour in marble burying and altered sociability in both the LMT and three-chamber test. These phenotypes mirror the cognitive and social deficits that define Helsmoortel-Van der Aa syndrome, including mild to severe intellectual delays, anxiety, attention-deficits, and obsessive-compulsive behaviours.[16] By apparent analogy, frameshift mice showed pronounced anxiety-like responses, as they spent less time in the open arms during elevated plus maze testing. Given that *ADNP* ranks among the most frequently mutated autism risk genes,[88] repetitive and socially altered behaviours in these mice reinforce the gene's role in ASD-associated neurodevelopmental disorders.[89]

Neuroanatomical analysis identified structural alterations in five brain regions, including a reduced motor cortex, cerebellar granular layer, and pontine nuclei volume, changes consistent with impaired motor function,[90] reflected by slower locomotion in the LMT and swimming performance in the MWM test. Thalamic area reductions and thalamocortical dysconnectivity, features previously linked to autism and cognitive deficits in rodents and humans,[91,92] were likewise observed. Enlarged hippocampal pyramidal neurons resembled abnormalities reported in a valproate-induced rat model of autism,[93] suggesting altered synaptic plasticity. Moreover, reduced neuronal density in the visual cortex and increased microglial cells in the somatosensory cortex pointed to inflammatory dysregulation without changes in astrocyte numbers. Neuron-specific AAV-mediated *Adnp* knockdown produced pro-inflammatory transcriptional signatures and microglial cell activation without neuronal loss,[94] likely due to postnatal induction at four weeks, contrasting with the embryonic onset of the *Adnp* frameshift mouse model. Similarly, $Cd4^{Cre}$ x $Adnp^{fl/fl}$ mice exhibited defective T-helper 2 cell responses,[27] aligning with recurrent infections seen in patients[16] and reflected by a pro-inflammatory transcriptome signature in a Helsmoortel-Van der Aa autopsy case.[12]

Mice lacking all *Adnp* exons (Δexons 1–6) demonstrated cognitive deficits in the MWM test,[25] consistent with those reported in a neuron-specific *Adnp* knockdown model.[94] In addition, plasma cortisol levels and splenic *Adnp* expression correlated with cognition and anxiety-related behaviour, suggesting systemic roles for Adnp.[95] Social impairments were similarly observed in both haploinsufficient (Δexons 1–6)[33] and p.Tyr718* mutant mice,[26] although not reproduced in the AAV-mediated knockdown model.[94] Motor deficits, including sex-specific gait alterations, were reported across haploinsufficient (Δexons 1–6) and p.Tyr718* models,[26,33,96] parallelling motor delays typical for Helsmoortel-Van der Aa syndrome patients.[16,17,97]

In this frameshift mouse model, the Adnp protein predominantly localised to the nucleus across multiple brain regions. However, during cellular differentiation, Adnp has been reported to translocate to the cytoplasm in cultured cells.[76,80] The heterozygous 14-bp deletion altered Adnp protein expression in both chromatin-enriched and cytoskeletal cortical fractions, suggesting functional crosstalk between nuclear and cytoskeletal compartments. We note that, because the fractionation approach is based on differential centrifugation, a small degree of cross-contamination between compartments may occur, and therefore these findings should be interpreted with this technical nuance in mind. Together, these results support a moonlighting function for Adnp, characterised by a predominant nuclear localisation and chromatin regulatory role that also influences cytoskeletal gene and protein expression. Adnp contains a bipartite NLS sequence,[5] and while a nuclear export signal has been predicted, it still awaits experimental confirmation.[24] Its cytoplasmic functions likely involve the SxIP motif within the neuroprotective NAP sequence, which binds to the microtubule end-binding proteins EB1/3,[98,99] or the protein's interactions with the nucleocytoplasmic shuttling protein 14-3-3.[80] Notably, multiple processed Adnp fragments were detected in cytoplasmic, membrane, and cytoskeletal protein fractions in frameshift mice, consistent with prior observations in total protein extracts, raising the possibility

that these fragments contribute to cytoskeletal associations.[52]

Transcriptomic profiling revealed a central role of Adnp in the regulation of Wnt signalling, a pathway essential for neuronal differentiation. Consistent with this, we previously observed increased HP1β and decreased β-catenin protein levels in the cerebellum of a Helsmoortel-Van der Aa syndrome autopsy case, confirming the translational relevance of the frameshift mouse model.[12] In the current study, frameshift mice showed altered expression of TFs involved in neuronal lineage specification, mirroring perturbations identified both in the human autopsy brain[12] and in homozygous mESCs, where Adnp deficiency disrupts neuronal differentiation.[48,76] The *in vivo* transcriptomic signature thus reflects these differentiation-related processes, suggesting that the *Adnp* frameshift variant leaves a persistent molecular imprint extending into neuronal maturity.

Mechanistically, Adnp directly interacts with the armadillo domain of β-catenin (residues 151–666) through its N-terminal region (residues 1–685) to regulate neuronal differentiation in mESCs.[76] Notably, the NAP motif of Adnp, when fused to a Flag-tag, retained β-catenin binding capacity, underscoring its functional relevance.[76] Consistent with human findings, reduced Wnt signalling has been linked to altered tooth development in patient-derived lymphoblastoid cell lines,[87] parallelling the dental malocclusion observed in frameshift mice and *Adnp* haploinsufficient (Δexons 1–6) mice.[87]

Proteomic analysis further revealed increased levels of the chromatin regulators HP1β and Smarcc2 in HET mice, in line with findings from the Helsmoortel-Van der Aa syndrome autopsy.[12] HP1β (Cbx1) is critical for genome stability, neocortical development, and neuromuscular junctions,[100] neural crest specification,[101] and its downregulation normally accompanies neuronal maturation.[102] Elevated HP1β levels in *Adnp* frameshift mouse brains could therefore reflect a retained immature neuronal state. Similarly, increased Smarcc2 abundance is characteristic of the transition from neural progenitor to neuronal BAF complexes,[103] further suggesting incomplete differentiation in *Adnp* deficient murine brains.

Integration of transcriptomic and proteomic data indicates that the *Adnp* frameshift variant drives actin dysregulation. Cytoskeletal deficits were initially attributed to the NAP (SxIP) motif of ADNP, which binds EB1/EB3 to promote microtubule assembly and neurite outgrowth while protecting neuroglia from toxic stress.[104,105] In addition, the NAP domain also contains an SH3-binding site mediating indirect interactions with the actin cytoskeleton.[13] Overexpression of autism-associated truncating variants such as the p.Glu830-synfs*83 variant, adjacent to the murine p.Leu822Hisfs*6 variant, impairs EB3 activity at microtubule plus-ends *in vitro*.[13]

Recently, Adnp was shown to interact indirectly with the NAD^+-dependent deacetylase Sirt1 through EB1/EB3, regulating Wnt signalling and mitophagy, underscoring crosstalk between nuclear and cytoskeletal compartments.[12] Importantly, a dual chromatin-cytoskeletal role was already seen in the histone methyltransferase SET-domain-containing 2 (SETD2), variants of which cause a neurodevelopmental disorder characterised by ID, motor deficits, and multisystem involvement,[106] features reminiscent of Helsmoortel-Van der Aa syndrome.[16] SETD2 mediates α-tubulin Lys40 methylation and regulates mRNA splicing[107] and DNA repair.[108] Similarly, ADNP contributes to CpG methylation of cytoskeletal genes in patient brain tissue[12] and has been implicated in RNA splicing and DNA repair.[109–111]

The actin cytoskeleton is crucial for synapse formation, plasticity, and neurotransmitter release.[112] Consistent with this, synaptic plasticity emerged as the most downregulated process in the brains of frameshift mice, with Adnp showing interactions with key regulators of synaptic plasticity, such as Dbn1 and Camk2a. Dbn1 overexpression modifies dendritic spine morphology,[113] while haploinsufficient *Adnp* mice (Δexon 6) exhibited Camk2a hyperphosphorylation and excessive long-term potentiation, normalised by Camk2a inhibition.[28] Collectively, these data underscore Adnp's dual role in chromatin and cytoskeletal regulation, linking impaired Wnt signalling and synaptic dysfunction.

Given Adnp's established chromatin-associated function,[4] we next examined how the *Adnp* frameshift variant affects chromatin architecture. Adnp interacts directly with HP1 in murine teratocarcinoma P19 cells[32] and associates with multiple chromatin remodelling complexes.[2,6,10,12,27,44,48,51,114] Chromatin conformation analyses in frameshift mice revealed no genome-wide chromatin architectural alterations, aligning with observations in *Adnp* homozygous mESCs.[9] Instead, local chromatin architectural changes correlated with transcriptomic differences, confirming that disruption of the ChAHP complex alters chromatin topology at specific loci rather than genome wide. In contrast, conditional *Chd4* knockout in cerebellar granular neurons caused a genome-wide increase in chromatin accessibility and cohesin recruitment to enhancers, highlighting that Adnp loss exerts a more localised architectural impact.[115] Because the frameshift variant reduces Adnp abundance in chromatin-enriched fractions, we observed a genome-wide increase in chromatin accessibility by ATAC-seq, consistent with findings in *Adnp* homozygous mESCs.[51] Cytoskeletal disruption may further influence nuclear chromatin accessibility through chromatocytoskeletal

remodelling.[116] Beyond its cytoplasmic structural role, nuclear actin and actin-related proteins participate in chromatin remodelling complexes, regulating gene accessibility during neuronal differentiation and cell–fate transitions.[117–119] Thus, Adnp-dependent chromatin accessibility changes likely integrate both chromatin and actin dynamics.

No effective therapy currently exists for Helsmoortel-Van der Aa syndrome patients.[4,120] However, the transcriptomic dataset from *Adnp* frameshift mouse brains highlights downregulated Wnt signalling as a potential therapeutic target for intervention. Wnt pathway modulation has shown promise in preclinical models of Alzheimer's disease[121,122] and Down syndrome,[123] suggesting translational relevance for Helsmoortel-Van der Aa syndrome.[124] Using the LMT system, frameshift mice displayed reduced locomotion, exploration, social interaction, and increased isolated behaviour. Therefore, combining LMT behavioural tracking with pharmacological modulation could provide a rapid, scalable method to evaluate candidate treatments and quantify both primary and secondary phenotypic improvements within 24 h of treatment.[40] Given the convergent cytoskeletal deficits observed in the transcriptomic and proteomic datasets of *Adnp* frameshift mouse brains, agents stabilising the cytoskeleton, such as the investigational ADNP-derived drug candidate NAP (davunetide), warrant evaluation in this disease-relevant mouse model.[124]

In summary, comprehensive molecular and behavioural characterisation of mice harbouring the heterozygous p.Leu822Hisfs*6 frameshift variant, connects behavioural dysfunctions with neuroanatomical brain alterations and chromatocytoskeletal pathways disruption, strikingly mirroring patient phenotypes. The combined transcriptomic and proteomic data illustrates the Wnt-actin regulatory axis central to Helsmoortel-Van der Aa syndrome and establishes a framework for targeted therapeutic exploration.

Caveats and limitations

This study employs a mouse model carrying a heterozygous *Adnp* frameshift variant in a C-terminal mutational hotspot, parallelling recurrent pathogenic variants observed in patients with Helsmoortel-Van der Aa syndrome.[16] Notably, the frameshift variant modelled in this study (c.2463_2476del; p.Leu822Hisfs*6) is an engineered mutation and has not yet been identified in patients. However, it is positioned within a C-terminal mutational hotspot and was designed to approximate recurrent pathogenic variants associated with Helsmoortel-Van der Aa syndrome.[16] By integrating chromatin accessibility, transcriptomics, proteomics, neuroanatomical analyses, and comprehensive behavioural testing, the study provides a multidimensional characterisation of ADNP-associated disease mechanisms. All molecular and behavioural datasets were generated with sample sizes consistent with established norms in preclinical molecular studies, providing statistical power comparable to similar preclinical studies. The convergence of molecular signatures with structural and behavioural phenotypes strengthens the internal coherence of the findings and reinforces the translational relevance of the model.

Several features intrinsic to the study design provide important context for interpretation. The experiments focused exclusively on male mice. Inclusion of females in future studies will allow assessment of potential sex-dependent modifiers, particularly given limited human data on sex differences.[16,17] Subclinical health variations in HET mice, including reduced body weight, recurrent infections, and dental malocclusion, together with technical nuances in protein fractionation that may permit minor cross-contamination between subcellular fractions, could subtly influence molecular and behavioural readouts. In particular, reduced body weight may influence performance in tasks with a motor component,[125] and its potential contribution to specific outcomes should be considered when interpreting genotype-related effects. Genome-wide chromatin architecture appeared largely preserved, although local changes in accessibility may reflect interactions between nuclear and cytoskeletal dynamics, highlighting the complexity of chromatocytoskeletal interplay. Observations such as cytoplasmic Adnp fragments and nuclear–cytoskeletal interactions remain mechanistically inferred and will benefit from further targeted validation. Finally, while transcriptomic and proteomic analyses highlight dysregulated Wnt and cytoskeletal pathways as promising therapeutic targets, functional intervention studies will be necessary to establish causality and translational potential.

Contributors

C.P.D. maintained the mouse colony, conceptualised experiments, performed and analysed most of the studies, wrote the manuscript text, and prepared all figures. E.C. maintained the mouse colony, contributed to the initial design of selected experiments, and performed behavioural testing, including the marble burying test. F.P. generated the Hi-C libraries, performed the Hi-C and ATAC-seq data analyses, prepared the final figures, wrote the corresponding Methods sections, and supervised the results of these experiments. M.B.V.D.L. conducted the LMT experiments and assisted with the graphical and statistical processing of behavioural data. D.A. facilitated LMT data analysis and assisted with figure visualisation. C.M.A. performed neuronal, microglial, and astrocytic staining and quantified results. D.S. performed the synaptoneurosome isolation for the revision experiments, glutamate stimulation, and Western Blot analysis of Camk2a. E.E. conducted mouse genotyping and RT-PCR gene expression assays under the supervision of C.P.D.; K.D.M. and A.K. participated in protein subcellular fractionation and molecular modelling experiments under C.P.D.'s supervision. J.H. assisted with mouse colony maintenance. S.T., I.P., and M.V. contributed to immunohistochemical staining and quantification of Adnp in all brain sections. E.C., D.V.D., and P.P.D.D. coordinated behavioural testing. S.N. and B.Y. performed neuroanatomical assessments. T.H. and I.H. generated the mouse line. L.M. provided

bioinformatic analysis of RNA sequencing data. G.C. initiated the experimental design for the Hi-C experiments. E.P. designed neuronal, microglial, and astrocytic staining experiments and participated in synaptoneurosome isolation. W.V.D.B. reviewed the manuscript. R.F.K. supervised the project, conceptualised experiments with C.P.D., and reviewed the manuscript. C.P.D., W.V.D.B., and R.F.K. acquired funding. Data verification: C.P.D., F.P., and D.A. accessed and verified the underlying data. All authors read and approved the final version of the manuscript.

Data sharing statement

The 14-bp deletion *Adnp* mouse model has been deposited at The Jackson Laboratory as *C57BL/6-Adnp*^{em1Ant}*/J* with strain #033128 with financial and logistic support from the Simons Foundation Autism Research Initiative (SFARI). The RNA-seq, ATAC-seq, and Hi-C datasets generated in this study have been deposited in the Gene Expression Omnibus (GEO) under accession number GSE319683. Mass spectrometry proteomics data have been deposited in the ProteomeXchange Consortium via the PRIDE partner repository under accession number PXD07459. All other data supporting the findings of this study are available within the article and its supplementary information files.

Declaration of interests

The authors declare no competing interests. This statement reflects all disclosures in accordance with the ICMJE guidelines.

Acknowledgements

We are grateful to all families who contributed to the broader research efforts underlying this work. We extend our sincere thanks to our students Kaoutar Choukri, Kristy Szrama, Lina Bastini, Eline Quirijnen, Tessa Nuyttens, Eline Kees, Kim Van Meel, and Amber Buys for their valuable contributions as part of their thesis projects. We are grateful to Prof. Dr. Chris Van Ginneken for her expert assistance in the assessment of ocular abnormalities and dental malformations. We acknowledge Karin Schildermans (Centre for Proteomics, CfP, University of Antwerp) for her support with LFQ-MS experiments and data analysis. Finally, we thank the Simons Foundation Autism Research Initiative (SFARI) for their assistance with the transport, import, and logistics of the mouse model.

Appendix A. Supplementary data

Supplementary data related to this article can be found at https://doi.org/10.1016/j.ebiom.2026.106309.

References

1 Pinhasov A, Mandel S, Torchinsky A, et al. Activity-dependent neuroprotective protein: a novel gene essential for brain formation. *Brain Res Dev Brain Res*. 2003;144(1):83–90.
2 Clémot-Dupont S, Lourenço Fernandes JA, Larrigan S, et al. The chromatin remodeler ADNP regulates neurodevelopmental disorder risk genes and neocortical neurogenesis. *Proc Natl Acad Sci U S A*. 2025;122(3):e2405981122.
3 Bassan M, Zamostiano R, Davidson A, et al. Complete sequence of a novel protein containing a femtomolar-activity-dependent neuroprotective peptide. *J Neurochem*. 1999;72(3):1283–1293.
4 D'Incal CP, Van Rossem KE, De Man K, et al. Chromatin remodeler Activity-Dependent Neuroprotective Protein (ADNP) contributes to syndromic autism. *Clin Epigenetics*. 2023;15(1):45.
5 Cappuyns E, Huyghebaert J, Vandeweyer G, Kooy RF. Mutations in ADNP affect expression and subcellular localization of the protein. *Cell Cycle*. 2018;17(9):1068–1075.
6 Mandel S, Gozes I. Activity-dependent neuroprotective protein constitutes a novel element in the SWI/SNF chromatin remodeling complex. *J Biol Chem*. 2007;282(47):34448–34456.
7 Mosch K, Franz H, Soeroes S, Singh PB, Fischle W. HP1 recruits activity-dependent neuroprotective protein to H3K9me3 marked pericentromeric heterochromatin for silencing of major satellite repeats. *PLoS One*. 2011;6(1):e15894.
8 Rosnoblet C, Vandamme J, Völkel P, Angrand P-O. Analysis of the human HP1 interactome reveals novel binding partners. *Biochem Biophys Res Commun*. 2011;413(2):206–211.
9 Kaaij LJT, Mohn F, van der Weide RH, de Wit E, Bühler M. The ChAHP complex counteracts chromatin looping at CTCF sites that emerged from SINE expansions in mouse. *Cell*. 2019;178(6):1437–1451.e14.
10 D'Incal CP, Van Rossem KE, Cappuyns E, et al. ADNP exhibits methyltransferase activity in overexpression systems and modulates DNA and histone methylation. *Autism Res*. 2025;18(11):2174–2191.
11 Merenlender-Wagner A, Malishkevich A, Shemer Z, et al. Autophagy has a key role in the pathophysiology of schizophrenia. *Mol Psychiatry*. 2015;20(1):126–132.
12 D'Incal C, Van Dijck A, Ibrahim J, et al. ADNP dysregulates methylation and mitochondrial gene expression in the cerebellum of a Helsmoortel-Van der Aa syndrome autopsy case. *Acta Neuropathol Commun*. 2024;12(1):62.
13 Ivashko-Pachima Y, Ganaiem M, Ben-Horin-Hazak I, et al. SH3- and actin-binding domains connect ADNP and SHANK3, revealing a fundamental shared mechanism underlying autism. *Mol Psychiatry*. 2022;27(8):3316–3327.
14 Helsmoortel C, Vulto-van Silfhout AT, Coe BP, et al. A SWI/SNF-related autism syndrome caused by de novo mutations in ADNP. *Nat Genet*. 2014;46(4):380–384.
15 Vandeweyer G, Helsmoortel C, Van Dijck A, et al. The transcriptional regulator ADNP links the BAF (SWI/SNF) complexes with autism. *Am J Med Genet C Semin Med Genet*. 2014;166(3):315–326.
16 Van Dijck A, Vulto-van Silfhout AT, Cappuyns E, et al. Clinical presentation of a complex neurodevelopmental disorder caused by mutations in *ADNP*. *Biol Psychiatry*. 2019;85(4):287–297.
17 Harutyunyan L, D'Incal CP, Jansen AC, Meuwissen M, Van Dijck A, Kooy RF. A systematic review illustrates the expanding clinical and molecular landscape of helsmoortel-van der Aa syndrome. *Brain Sci*. 2025;16(1):4.
18 Bend EG, Aref-Eshghi E, Everman DB, et al. Gene domain-specific DNA methylation episignatures highlight distinct molecular entities of ADNP syndrome. *Clin Epigenetics*. 2019;11(1):64.
19 Breen MS, Garg P, Tang L, et al. Episignatures stratifying helsmoortel-van der Aa syndrome show modest correlation with phenotype. *Am J Hum Genet*. 2020;107(3):555–563.
20 Dingemans AJM, Hinne M, Truijen KMG, et al. PhenoScore quantifies phenotypic variation for rare genetic diseases by combining facial analysis with other clinical features using a machine-learning framework. *Nat Genet*. 2023;55(9):1598–1607.
21 Bieluszewska A, Wulfridge P, Fang K-C, et al. Transcriptomic analysis uncovers an unfolded protein response in ADNP syndrome. *Mol Cell Biol*. 2025;45(4):143–153.
22 Mandel S, Spivak-Pohis I, Gozes I. ADNP differential nucleus/cytoplasm localization in neurons suggests multiple roles in neuronal differentiation and maintenance. *J Mol Neurosci*. 2008;35(2):127–141.
23 Gennet N, Herden C, Bubb VJ, Quinn JP, Kipar A. Expression of activity-dependent neuroprotective protein in the brain of adult rats. *Histol Histopathol*. 2008;23(3):309–317.
24 Furman S, Steingart RA, Mandel S, Hauser JM, Brenneman DE, Gozes I. Subcellular localization and secretion of activity-dependent neuroprotective protein in astrocytes. *Neuron Glia Biol*. 2004;1(3):193–199.
25 Vulih-Shultzman I, Pinhasov A, Mandel S, et al. Activity-dependent neuroprotective protein snippet NAP reduces tau hyperphosphorylation and enhances learning in a novel transgenic mouse model. *J Pharmacol Exp Ther*. 2007;323(2):438–449.
26 Karmon G, Sragovich S, Hacohen-Kleiman G, et al. Novel ADNP syndrome mice reveal dramatic sex-specific peripheral gene expression with brain synaptic and tau pathologies. *Biol Psychiatry*. 2022;92(1):81–95.
27 Ferreira ACF, Szeto ACH, Clark PA, et al. Neuroprotective protein ADNP-dependent histone remodeling complex promotes T helper 2 immune cell differentiation. *Immunity*. 2023;56(7):1468–1484.e7.
28 Cho H, Yoo T, Moon H, et al. Adnp-mutant mice with cognitive inflexibility, CaMKIIα hyperactivity, and synaptic plasticity deficits. *Mol Psychiatry*. 2023;28(8):3548–3562.
29 Horii T, Arai Y, Yamazaki M, et al. Validation of microinjection methods for generating knockout mice by CRISPR/Cas-mediated genome engineering. *Sci Rep*. 2014;4:4513.
30 Horii T, Morita S, Kimura M, Terawaki N, Shibutani M, Hatada I. Efficient generation of conditional knockout mice via sequential introduction of lox sites. *Sci Rep*. 2017;7(1):7891.

31 Furman S, Hill JM, Vulih I, et al. Sexual dimorphism of activity-dependent neuroprotective protein in the mouse arcuate nucleus. *Neurosci Lett*. 2004;373(1):73–78.
32 Mandel S, Rechavi G, Gozes I. Activity-dependent neuroprotective protein (ADNP) differentially interacts with chromatin to regulate genes essential for embryogenesis. *Dev Biol*. 2007;303(2):814–824.
33 Hacohen-Kleiman G, Sragovich S, Karmon G, et al. Activity-dependent neuroprotective protein deficiency models synaptic and developmental phenotypes of autism-like syndrome. *J Clin Invest*. 2018;128(11):4956–4969.
34 Gompers AL, Su-Feher L, Ellegood J, et al. Germline Chd8 haploinsufficiency alters brain development in mouse. *Nat Neurosci*. 2017;20(8):1062–1073.
35 Collins SC, Wagner C, Gagliardi L, et al. A method for parasagittal sectioning for neuroanatomical quantification of brain structures in the adult mouse. *Curr Protoc Mouse Biol*. 2018;8(3):e48.
36 Mikhaleva A, Kannan M, Wagner C, Yalcin B. Histomorphological phenotyping of the adult mouse brain. *Curr Protoc Mouse Biol*. 2016;6(3):307–332.
37 Collins SC, Mikhaleva A, Vrcelj K, et al. Large-scale neuroanatomical study uncovers 198 gene associations in mouse brain morphogenesis. *Nat Commun*. 2019;10(1):3465.
38 Van Leuven W, Van Dam D, Moens L, De Deyn PP, Dewilde S. A behavioural study of neuroglobin-overexpressing mice under normoxic and hypoxic conditions. *Biochim Biophys Acta*. 2013;1834(9):1764–1771.
39 van der Werf IM, Van Dam D, Missault S, et al. Behavioural characterization of AnkyrinG deficient mice, a model for ANK3 related disorders. *Behav Brain Res*. 2017;328:218–226.
40 de Chaumont F, Ey E, Torquet N, et al. Real-time analysis of the behaviour of groups of mice via a depth-sensing camera and machine learning. *Nat Biomed Eng*. 2019;3(11):930–942.
41 Yin Z, Valkenburg F, Hornix BE, et al. Progressive motor deficit is mediated by the denervation of neuromuscular junctions and axonal degeneration in transgenic mice expressing mutant (P301S) tau protein. *J Alzheimers Dis*. 2017;60(s1):S41–S57.
42 Schurch NJ, Schofield P, Gierliński M, et al. How many biological replicates are needed in an RNA-seq experiment and which differential expression tool should you use? *RNA*. 2016;22(6):839–851.
43 Yshii L, Pasciuto E, Bielefeld P, et al. Astrocyte-targeted gene delivery of interleukin 2 specifically increases brain-resident regulatory T cell numbers and protects against pathological neuroinflammation. *Nat Immunol*. 2022;23(6):878–891.
44 Hadar A, Kapitansky O, Ganaiem M, et al. Introducing ADNP and SIRT1 as new partners regulating microtubules and histone methylation. *Mol Psychiatry*. 2021;26(11):6550–6561.
45 De Rubeis S, Pasciuto E, Li KW, et al. CYFIP1 coordinates mRNA translation and cytoskeleton remodeling to ensure proper dendritic spine formation. *Neuron*. 2013;79(6):1169–1182.
46 Charalambous DC, Pasciuto E, Mercaldo V, et al. KIF1Bβ transports dendritically localized mRNPs in neurons and is recruited to synapses in an activity-dependent manner. *Cell Mol Life Sci*. 2013;70(2):335–356.
47 Peng H, Wang H, Kong W, Li J, Goh WWB. Optimizing differential expression analysis for proteomics data via high-performing rules and ensemble inference. *Nat Commun*. 2024;15(1):3922.
48 Ostapcuk V, Mohn F, Carl SH, et al. Activity-dependent neuroprotective protein recruits HP1 and CHD4 to control lineage-specifying genes. *Nature*. 2018;557(7707):739–743.
49 Ahel J, Pandey A, Schwaiger M, et al. ChAHP2 and ChAHP control diverse retrotransposons by complementary activities. *Genes Dev*. 2024;38(11–12):554–568.
50 Bonev B, Mendelson Cohen N, Szabo Q, et al. Multiscale 3D genome rewiring during mouse neural development. *Cell*. 2017;171(3):557–572.e24.
51 Sun X, Yu W, Li L, Sun Y. ADNP controls gene expression through local chromatin architecture by association with BRG1 and CHD4. *Front Cell Dev Biol*. 2020;8:553.
52 D'Incal CP, Cappuyns E, Choukri K, et al. Tracing the invisible mutant ADNP protein in Helsmoortel-Van der Aa syndrome patients. *Sci Rep*. 2024;14(1):14710.
53 Langmead B, Salzberg SL. Fast gapped-read alignment with Bowtie 2. *Nat Methods*. 2012;9(4):357–359.
54 Li H, Handsaker B, Wysoker A, et al. The sequence alignment/Map format and SAMtools. *Bioinformatics*. 2009;25(16):2078–2079.
55 Tarasov A, Vilella AJ, Cuppen E, Nijman IJ, Prins P. Sambamba: fast processing of NGS alignment formats. *Bioinformatics*. 2015;31(12):2032–2034.
56 Ramírez F, Dündar F, Diehl S, Grüning BA, Manke T. deepTools: a flexible platform for exploring deep-sequencing data. *Nucleic Acids Res*. 2014;42(W1):W187–W191.
57 Robinson JT, Thorvaldsdottir H, Turner D, Mesirov JP. igv.js: an embeddable JavaScript implementation of the Integrative Genomics Viewer (IGV). *Bioinformatics*. 2023;39(1):btac830.
58 Zhang Y, Liu T, Meyer CA, et al. Model-based analysis of ChIP-Seq (MACS). *Genome Biol*. 2008;9(9):R137.
59 Schindelin J, Arganda-Carreras I, Frise E, et al. Fiji: an open-source platform for biological-image analysis. *Nat Methods*. 2012;9(7):676–682.
60 Van Dam D, Valkenburg F, Van Kolen K, Pintelon I, Timmermans J-P, De Deyn PP. Behavioral and neuropathological phenotyping of the Tau58/2 and Tau58/4 transgenic mouse models for FTDP-17. *Life (Basel)*. 2023;13(10):2088.
61 Liao Y, Smyth GK, Shi W. featureCounts: an efficient general purpose program for assigning sequence reads to genomic features. *Bioinformatics*. 2014;30(7):923–930.
62 Akhmedov M, Martinelli A, Geiger R, Kwee I. Omics Playground: a comprehensive self-service platform for visualization, analytics and exploration of Big Omics Data. *NAR Genom Bioinform*. 2020;2(1):lqz019.
63 Zhou Y, Zhou B, Pache L, et al. Metascape provides a biologist-oriented resource for the analysis of systems-level datasets. *Nat Commun*. 2019;10(1):1523.
64 Nott A, Schlachetzki JCM, Fixsen BR, Glass CK. Nuclei isolation of multiple brain cell types for omics interrogation. *Nat Protoc*. 2021;16(3):1629–1646.
65 Servant N, Varoquaux N, Lajoie BR, et al. HiC-Pro: an optimized and flexible pipeline for Hi-C data processing. *Genome Biol*. 2015;16:259.
66 Abdennur N, Mirny LA. Cooler: scalable storage for Hi-C data and other genomically labeled arrays. *Bioinformatics*. 2020;36(1):311–316.
67 Kerpedjiev P, Abdennur N, Lekschas F, et al. HiGlass: web-based visual exploration and analysis of genome interaction maps. *Genome Biol*. 2018;19(1):125.
68 Ramírez F, Bhardwaj V, Arrigoni L, et al. High-resolution TADs reveal DNA sequences underlying genome organization in flies. *Nat Commun*. 2018;9(1):189.
69 Open2C, Abdennur N, Abraham S, et al. Cooltools: enabling high-resolution Hi-C analysis in Python. *PLoS Comput Biol*. 2024;20(5):e1012067.
70 Roayaei Ardakany A, Gezer HT, Lonardi S, Ay F. Mustache: multi-scale detection of chromatin loops from Hi-C and Micro-C maps using scale-space representation. *Genome Biol*. 2020;21(1):256.
71 Flyamer IM, Illingworth RS, Bickmore WA. Coolpup.py: versatile pile-up analysis of Hi-C data. *Bioinformatics*. 2020;36(10):2980–2985.
72 Aboonq MS, Vasiliou SA, Haddley K, Quinn JP, Bubb VJ. Activity-dependent neuroprotective protein modulates its own gene expression. *J Mol Neurosci*. 2012;46(1):33–39.
73 Kilpinen S, Heliölä H, Achim K. Range of chromatin accessibility configurations are permissive of GABAergic fate acquisition in developing mouse brain. *BMC Genomics*. 2023;24(1):725.
74 Klune CB, Jin B, DeNardo LA. Linking mPFC circuit maturation to the developmental regulation of emotional memory and cognitive flexibility. *Elife*. 2021;10:e64567.
75 Yang X, Matsuda K, Bialek P, et al. ATF4 is a substrate of RSK2 and an essential regulator of osteoblast biology; implication for Coffin-Lowry Syndrome. *Cell*. 2004;117(3):387–398.
76 Sun X, Peng X, Cao Y, Zhou Y, Sun Y. ADNP promotes neural differentiation by modulating Wnt/β-catenin signaling. *Nat Commun*. 2020;11(1):2984.
77 Lucchesi W, Mizuno K, Giese KP. Novel insights into CaMKII function and regulation during memory formation. *Brain Res Bull*. 2011;85(1–2):2–8.
78 Nair RR, Patil S, Tiron A, et al. Dynamic arc SUMOylation and selective interaction with F-Actin-Binding protein drebrin A in LTP consolidation in vivo. *Front Synaptic Neurosci*. 2017;9:8.
79 Sragovich S, Malishkevich A, Piontkewitz Y, et al. The autism/neuroprotection-linked ADNP/NAP regulate the excitatory glutamatergic synapse. *Transl Psychiatry*. 2019;9(1):2.

80 Bennison SA, Blazejewski SM, Liu X, et al. The cytoplasmic localization of ADNP through 14-3-3 promotes sex-dependent neuronal morphogenesis, cortical connectivity, and calcium signaling. *Mol Psychiatry*. 2023;28(5):1946–1959.
81 Carlyle BC, Kitchen RR, Kanyo JE, et al. A multiregional proteomic survey of the postnatal human brain. *Nat Neurosci*. 2017;20(12):1787–1795.
82 Zhang Y, See YX, Tergaonkar V, Fullwood MJ. Long-Distance repression by human silencers: chromatin interactions and phase separation in silencers. *Cells*. 2022;11(9):1560.
83 Wang B, Ji L, Bian Q. SATB1 regulates 3D genome architecture in T cells by constraining chromatin interactions surrounding CTCF-binding sites. *Cell Rep*. 2023;42(4):112323.
84 Ramanujam PL, Mehrotra S, Kumar RP, et al. Global chromatin organizer SATB1 acts as a context-dependent regulator of the Wnt/Wg target genes. *Sci Rep*. 2021;11(1):3385.
85 Zelenka T, Klonizakis A, Tsoukatou D, et al. The 3D enhancer network of the developing T cell genome is shaped by SATB1. *Nat Commun*. 2022;13(1):6954.
86 Maugeri G, D'Amico AG, Magrì B, Musumeci G, D'Agata V. Activity-Dependent Neuroprotective Protein (ADNP): an overview of its role in the eye. *Int J Mol Sci*. 2022;23(21):13654.
87 Gozes I, Van Dijck A, Hacohen-Kleiman G, et al. Premature primary tooth eruption in cognitive/motor-delayed ADNP-mutated children. *Transl Psychiatry*. 2017;7(2):e1043.
88 Satterstrom FK, Kosmicki JA, Wang J, et al. Large-Scale exome sequencing study implicates both developmental and functional changes in the neurobiology of autism. *Cell*. 2020;180(3):568–584.e23.
89 Patterson PH. Modeling autistic features in animals. *Pediatr Res*. 2011;69(5 Part 2):34R–40R.
90 Lopes G, Nogueira J, Dimitriadis G, Menendez JA, Paton JJ, Kampff AR. A robust role for motor cortex. *Front Neurosci*. 2023;17:971980.
91 Horata E, Ay H, Aslan D. Autistic-like behaviour and changes in thalamic cell numbers a rat model of valproic acid-induced autism; A behavioural and stereological study. *Brain Res*. 2024;1840:149047.
92 Thalhammer M, Schulz J, Scheulen F, et al. Distinct volume alterations of thalamic nuclei across the schizophrenia spectrum. *Schizophr Bull*. 2024;50(5):1208–1222.
93 Cloarec R, Riffault B, Dufour A, et al. Pyramidal neuron growth and increased hippocampal volume during labor and birth in autism. *Sci Adv*. 2019;5(1):eaav0394.
94 Conrow-Graham M, Williams JB, Martin J, et al. A convergent mechanism of high risk factors ADNP and POGZ in neurodevelopmental disorders. *Brain*. 2022;145(9):3250–3263.
95 Sragovich S, Ziv Y, Vaisvaser S, Shomron N, Hendler T, Gozes I. The autism-mutated ADNP plays a key role in stress response. *Transl Psychiatry*. 2019;9(1):235.
96 Kapitansky O, Karmon G, Sragovich S, et al. Single cell ADNP predictive of human muscle disorders: mouse knockdown results in muscle wasting. *Cells*. 2020;9(10):2320.
97 D'Incal CP, Annear DJ, Elinck E, et al. Loss-of-function of activity-dependent neuroprotective protein (ADNP) by a splice-acceptor site mutation causes Helsmoortel-Van der Aa syndrome. *Eur J Hum Genet*. 2024;32(6):630–638.
98 Oz S, Kapitansky O, Ivashco-Pachima Y, et al. The NAP motif of activity-dependent neuroprotective protein (ADNP) regulates dendritic spines through microtubule end binding proteins. *Mol Psychiatry*. 2014;19(10):1115–1124.
99 Ivashko-Pachima Y, Sayas CL, Malishkevich A, Gozes I. ADNP/NAP dramatically increase microtubule end-binding protein-Tau interaction: a novel avenue for protection against tauopathy. *Mol Psychiatry*. 2017;22(9):1335–1344.
100 Aucott R, Bullwinkel J, Yu Y, et al. HP1-beta is required for development of the cerebral neocortex and neuromuscular junctions. *J Cell Biol*. 2008;183(4):597–606.
101 Tien C-L, Mohammadparast S, Chang C. Heterochromatin protein 1 beta regulates neural and neural crest development by repressing pluripotency-associated gene pou5f3.2/oct25 in Xenopus. *Dev Dyn*. 2021;250(8):1113–1124.
102 Panteleeva I, Boutillier S, See V, et al. HP1alpha guides neuronal fate by timing E2F-targeted genes silencing during terminal differentiation. *EMBO J*. 2007;26(15):3616–3628.
103 Cornejo KG, Venegas A, Sono MH, et al. Activity-assembled nBAF complex mediates rapid immediate early gene transcription by regulating RNA polymerase II productive elongation. *Cell Rep*. 2024;43(11):114877.
104 Gozes I, Divinski I. The femtomolar-acting NAP interacts with microtubules: novel aspects of astrocyte protection. *J Alzheimers Dis*. 2005;6(s6):S37–S41.
105 Ashur-Fabian O, Segal-Ruder Y, Skutelsky E, et al. The neuroprotective peptide NAP inhibits the aggregation of the beta-amyloid peptide. *Peptides*. 2003;24(9):1413–1423.
106 Park IY, Powell RT, Tripathi DN, et al. Dual chromatin and cytoskeletal remodeling by SETD2. *Cell*. 2016;166(4):950–962.
107 Walker C, Burggren W. Remodeling the epigenome and (epi)cytoskeleton: a new paradigm for co-regulation by methylation. *J Exp Biol*. 2020;223(13):jeb220632.
108 Luscan A, Laurendeau I, Malan V, et al. Mutations in SETD2 cause a novel overgrowth condition. *J Med Genet*. 2014;51(8):512–517.
109 Rabin R, Radmanesh A, Glass IA, et al. Genotype-phenotype correlation at codon 1740 of SETD2. *Am J Med Genet A*. 2020;182(9):2037–2048.
110 Schirer Y, Malishkevich A, Ophir Y, Lewis J, Giladi E, Gozes I. Novel marker for the onset of frontotemporal dementia: early increase in activity-dependent neuroprotective protein (ADNP) in the face of Tau mutation. *PLoS ONE*. 2014;9(1):e87383.
111 Sigismondo G, Arseni L, Palacio-Escat N, Hofmann TG, Seiffert M, Krijgsveld J. Multi-layered chromatin proteomics identifies cell vulnerabilities in DNA repair. *Nucleic Acids Res*. 2023;51(2):687–711.
112 Gentile JE, Carrizales MG, Koleske AJ. Control of synapse structure and function by actin and its regulators. *Cells*. 2022;11(4):603.
113 Mizui T, Takahashi H, Sekino Y, Shirao T. Overexpression of drebrin A in immature neurons induces the accumulation of F-actin and PSD-95 into dendritic filopodia, and the formation of large abnormal protrusions. *Mol Cell Neurosci*. 2005;30(1):149–157.
114 Markenscoff-Papadimitriou E, Binyameen F, Whalen S, et al. Autism risk gene POGZ promotes chromatin accessibility and expression of clustered synaptic genes. *Cell Rep*. 2021;37(10):110089.
115 Goodman JV, Yamada T, Yang Y, et al. The chromatin remodeling enzyme Chd4 regulates genome architecture in the mouse brain. *Nat Commun*. 2020;11(1):3419.
116 Lewerissa EI, Nadif Kasri N, Linda K. Epigenetic regulation of autophagy-related genes: implications for neurodevelopmental disorders. *Autophagy*. 2024;20(1):15–28.
117 Mahmood SR, Xie X, Hosny El Said N, Venit T, Gunsalus KC, Percipalle P. β-actin dependent chromatin remodeling mediates compartment level changes in 3D genome architecture. *Nat Commun*. 2021;12(1):5240.
118 Sen B, Xie Z, Thomas MD, et al. Nuclear actin structure regulates chromatin accessibility. *Nat Commun*. 2024;15(1):4095.
119 Hu X, Liu ZZ, Chen X, et al. MKL1-actin pathway restricts chromatin accessibility and prevents mature pluripotency activation. *Nat Commun*. 2019;10(1):1695.
120 D'Incal CP, Mateiu L, De Man K, Elinck E, Gozes I, Kooy RF. The ADNP-Mediated transcriptome response to ketamine impairs the cytoskeletal protein axis. *J Mol Neurosci*. 2025;75(4):136.
121 Ding J, Lee S-J, Vlahos L, et al. Therapeutic blood-brain barrier modulation and stroke treatment by a bioengineered FZD4-selective WNT surrogate in mice. *Nat Commun*. 2023;14(1):2947.
122 Palomer E, Buechler J, Salinas PC. Wnt signaling deregulation in the aging and Alzheimer's brain. *Front Cell Neurosci*. 2019;13:227.
123 Granno S, Nixon-Abell J, Berwick DC, et al. Downregulated Wnt/β-catenin signalling in the down syndrome hippocampus. *Sci Rep*. 2019;9(1):7322.
124 Gozes I. The ADNP syndrome and CP201 (NAP) potential and hope. *Front Neurol*. 2020;11:608444.
125 Mao J-H, Langley SA, Huang Y, et al. Identification of genetic factors that modify motor performance and body weight using collaborative cross mice. *Sci Rep*. 2015;5:16247.